Sediment diffusion in deterministic non-equilibrium bed load transport simulations

Patricio Bohorquez[a,*], Christophe Ancey[b,**]

[a]*Área de Mecánica de Fluidos, Departamento de Ingeniería Mecánica y Minera, CEACTierra, Universidad de Jaén, Campus de las Lagunillas, 23071, Jaén, Spain*
[b]*Environmental Hydraulics Laboratory, École Polytechnique Fédérale de Lausanne, 1015 Lausanne, Switzerland*

Abstract

The objective of this paper is to examine the importance of sediment diffusion relative to advection in bed load transport. At moderate bottom shear stress, water turbulence is too weak for picking up and keeping particles in suspension and so shallow water flows over erodible slopes carry sediment as bed load. Two deterministic frameworks are routinely used for studying bed load transport in sedimentation engineering and computational river dynamics. In equilibrium theory, the sediment transport rate is directly related to the water discharge (or bottom shear stress) independently of the intensity of sediment transport and the flow conditions (nearly steady flow as well as non-uniform time-dependent flow); embodied in the Exner equation, the bedload transport equation dictates bed evolution. In non-equilibrium (or non-capacity sediment transport) theory, sediment transport results from the imbalance between particle entrainment and deposition. Generally, sediment diffusion is included in none of these approaches. Based on recent advances in the probabilistic theory of sediment transport, this paper emphasizes the part played by particle diffusion in bed load transport. In light of these new developments, we revisit the concepts of adaptation length and entrainment rate, two essential elements in the deterministic non-equilibrium bed load theory. Using the shallow water equations, we ran numerical simulations of channel degradation and anti-dune development in gravel bed streams over steep slopes, which showed that sediment diffusion is as significant as advection in flume experiments. The predictive capability of deterministic models can thus be improved by including diffusion in the governing equations. We also present a versatile numerical framework, which makes it possible to use either deterministic or stochastic formulations of bed load transport.

Keywords: Saint-Venant-Exner, Particle diffusion, Adaptation length, Aggradation/Degradation, Anti-dunes

1. Introduction

This article analyses the part played by particle diffusion in sediment transport by conducting nonlinear numerical simulations reproducing bed load experiments. The mainstream view has long been that particles are advected by the water flow, which explains why the sediment transport rate is mostly expressed as a function of the water discharge or the bottom shear stress. So the problem posed by particle diffusion has gone unnoticed

**Email address*: patricio.bohorquez@ujaen.es (P. Bohorquez)
***Email address*: christophe.ancey@epfl.ch (C. Ancey)

until very recently. Surprisingly enough, for other transport phenomena in turbulent flows (e.g., pollutant transport), it has long been recognised that particle diffusion plays a key role [1, 2]. Recently, new views have emerged and shown the significance of particle diffusion in bedload transport, especially under weak and partial bed load transport [3, 4, 5, 6, 7, 8]. Recent theoretical studies have also highlighted the diffusive nature of bed load transport and the influence of particle diffusion on the (stochastic) fluctuations of transport rates and particle concentration (hereafter called *particle activity*) [9, 10].

In this article we address the relative importance of diffusion and advection in the momentum balance equation. Here we use a 'simple' morphodynamic model consisting of the Saint-Venant-Exner equations. An innovative feature has been to supplement these deterministic equations with two further governing equations that describe the dynamics of sediment transport [10, 11]. The reader is referred to equations (1)–(4b) below to get an overview of the governing equations. One of these equations is a stochastic partial differential equation, which provides information on the particle ativity fluctuations. The deterministic components of the formulation used are equivalent to most common approaches to predicting bed load transport in shallow water flows, as shown in the first part of the article. The second part addresses the role of particle diffusion in bed load transport by running numerical simulations and comparing them with available theoretical solutions and experimental data.

The case studies considered in this article correspond to shallow water flows over erodible sloping beds in laboratory flumes that produce nearly one-dimensional flows (complicated structures such as alternate bars are not investigated). Laboratory studies have revealed that bedload transport exhibits a complex behaviour, even in the ideal case of an initially uniform flow in a sandy- or gravel-bed flume. For instance, Gilbert [12], a pioneer in the experimental investigation of bedload transport, observed the development of bed instabilities (ripples, dunes and anti-dunes). Later, Simons and Richardson [13] quantified the increase in head loss due to bed form roughness when the flow passed from the lower- to the upper-flow regime. Kennedy [14] found out the existence of multiple states in which upstream and downstream migrating anti-dunes coexisted with steady standing waves. Soni et al. [15] commented on the sediment transport rate fluctuations in transient aggradation processes. More recently, Ancey et al. [16] monitored stochastic fluctuations of the sediment transport rate in the laboratory while Naqshband et al. [17] and Cartigny et al. [18] described turbulent fluctuations of the sediment load with respect to the mean value as a result of bed form migration both in subcritical and supercritical flows, respectively. At last, Yager et al. [19] reviewed recent advances on bed surface structures and armour layer formation. There is no unified theoretical framework for predicting all of these complex phenomena even in the simplest case of well sorted sediments [20] and this explains why there is currently a large body of research on this emerging topic. Increasing the accuracy of model predictions at an affordable computational cost is an attractive challenge. In this respect, simple models such as flow-depth-averaged models (e.g., Saint-Venant-Exner equations) are still worth further investigation even though more refined models are now increasingly used [21].

1.1. Governing equations

We will use the following stochastic-deterministic Saint-Venant-Exner (sdSVE)

$$\frac{\partial h}{\partial t}+\frac{\partial h\bar{v}}{\partial x} = 0, \tag{1}$$

$$\frac{\partial h\bar{v}}{\partial t}+\frac{\partial h\bar{v}^2}{\partial x}+gh\frac{\partial h}{\partial x} = -gh\frac{\partial y_b}{\partial x}-\frac{f\,\bar{v}\,|\bar{v}|}{8}+\frac{\partial}{\partial x}\left(\nu h\frac{\partial \bar{v}}{\partial x}\right), \tag{2}$$

$$(1-\zeta_b)\frac{\partial y_b}{\partial t} = D-E, \tag{3}$$

in which $h(x,t)=y_s-y_b$ denotes the flow depth, $y_b(x,t)$ and $y_s(x,t)$ are the positions of the bed and free surfaces, $\bar{v}$ is the depth-averaged velocity, t is time, ϱ is the water density, f is the nondimensional Darcy-Weisbach friction factor, ζ_b the bed porosity, D and E represent the deposition and entrainment rates, respectively, and the extra term $\partial_x(\nu h\partial_x\bar{v})$ in the momentum balance equation (2) represents a simple depth-averaged Reynolds stress. We use a Cartesian frame $(x,\ y)$ in which x is the horizontal position and y is the (vertical) elevation. We supplement these classical equations with two additional equations:

$$\frac{\partial b}{\partial t}+\frac{\partial}{\partial x}(\bar{u}_s b)-\frac{\partial^2}{\partial x^2}(D_u b) = E'-D+\sqrt{2\mu b}\,\xi_b \tag{4a}$$

$$\frac{\partial}{\partial t}\langle\gamma\rangle+\frac{\partial}{\partial x}(\bar{u}_s\langle\gamma\rangle)-\frac{\partial^2}{\partial x^2}(D_u\langle\gamma\rangle) = E-D\,, \tag{4b}$$

where $\bar{u}_s$ is the mean particle velocity, D_u is the particle diffusivity, μ is the collective entrainment rate and ξ_b is a Gaussian noise term. In a former paper [10], it was shown that the number of moving particles per unit bed area, here called the *particle activity* γ (following Furbish' terminology), is a random variable, whose time variations can be calculated within the framework of jump Markov process. To gain analytical traction, the probability density function of γ can be studied using the Poisson representation—a kind of Fourier transform in the probability space [22]. The resulting variable is called the Poisson density b. Equation (4a) is the governing equation for b: this is a Langevin equation, which takes the form of an advection diffusion equation with a source term including coloured noise [10]. Itô's convention is used in our approach for defining and interpreting stochastic integration [22]. Taking the ensemble average of this equation leads to the governing equation (4b) for the mean particle activity $\langle\gamma\rangle$.

An interesting property of the Poisson representation (which was used to infer equation (4b) from (4a)) is that the moments of b and γ are linked

$$\langle\gamma\rangle=\frac{\langle b\rangle\,V_p}{B}\,. \tag{5}$$

The erosion and deposition rates (that will be introduced later) can be expressed as functions of the Poisson density b or the particle activity $\langle\gamma\rangle$. The stochastic and deterministic entrainment rates are related by $\langle E'\rangle = E\,B/V_p$ in which B is the channel width and V_p is the typical volume of one grain. Solving the Langevin equation (4a) for b allows us to fully characterize the fluctuations of the particle activity while solving the ensemble-averaged advection diffusion equation (4b) for $\langle\gamma\rangle$ provides information on the mean behaviour of the particle activity.

1.2. Definition of the sediment transport rate

An important element of sediment transport is the sediment transport rate $\bar{q}_s$. There is no unique definition of $\bar{q}_s$ [23, 24, 25]. Here we follow Furbish et al. [9] and define the bulk sediment transport rate as the sum of convective and diffusive contributions

$$\bar{q}_s = \bar{u}_s\langle\gamma\rangle - \frac{\partial}{\partial x}(D_u\langle\gamma\rangle)\,. \tag{6}$$

In the following, we will refer to the *advection transport rate* as $\bar{q}_{c,s} = \bar{u}_s\langle\gamma\rangle$ and the *diffusion transport rate* as $\bar{q}_{d,s} = -\partial_x\, D_u\langle\gamma\rangle$. Both contributions can be computed by solving the advection diffusion equation (4b) for the mean particle activity $\langle\gamma\rangle$. An alternative is to compute them by first solving the stochastic Langevin equation (4a) for the Poisson density b, then making use of equation (5) to deduce $\langle\gamma\rangle$. Note that the second contribution on the right-hand side of (6) is called the "diffusion transport rate" because it arises from the diffusion term in (4b), which can be recast as

$$\frac{\partial\,\bar{q}_s}{\partial x} = E - D - \frac{\partial\,\langle\gamma\rangle}{\partial t}\,, \tag{7}$$

even though the definition of $\bar{q}_{d,s}$ involves the spatial gradient of $\langle\gamma\rangle$.

An interesting feature of the sdSVE equations (1)–(4b) is that they can be viewed as a generalization of different approaches. On the one hand, the ensemble-averaged sdSVE equations (1)-(3), (4b) lead to the classical equation based on Einstein [26]'s bed load transport function under nearly steady uniform flow conditions (see Section 2.1). On the other hand, more involved bedload transport equations—which are referred to as non-equilibrium or non-capacity sediment transport equations, and are common to sedimentation engineering [27, 28]—are also a particular case of the mean sdSVE equations under unsteady, non-uniform flow conditions, see Sections 2.2-2.3. A noticeable consequence of this is that existing numerical codes can be readily adapted to evaluate the fluctuations of sediment transport rate by replacing equation (4b) with (4a). In practice, this requires adding the coloured noise term $\sqrt{2\mu b}\,\xi_b$ to the advection-diffusion equation and selecting an appropriate discretization technique of the stochastic partial differential equation (4a), e.g., see Bohorquez and Ancey [11] for detail on the numerical schemes. The diffusion term $-\partial_{xx}(D_u\, b)$ in equation (4a) is no longer negligible, which leads us to think that the predictive capability of non-equilibrium (or non-capacity) bedload transport equations can be improved by setting $D_u > 0$ in the diffusive term $-\partial_{xx}(D_u\,\langle\gamma\rangle)$ of the advection diffusion equation (4b), as shown later in this article.

1.3. Objectives

The present study focuses on the three following issues: (i) we revisit the concept of *adaptation length* within the framework of the sdSVE equations (1)-(4b), (ii) we seek a closure equation for the erosion-to-deposition-rate ratio, which covers a wide range of Shields numbers, from zero to very large values (i.e., from vanishingly low transport rates to the full mobility regime) [29, 30, 31], and (iii) we analyze the importance of particle diffusion relative to particle advection in different case studies, including the simulation of channel degradation in Newton [32]'s experiments and the numerical study of anti-dunes in gravel bed streams over steep slopes [33, 34, 35, 36].

The *adaptation length*, denoted by $\ell_{c,d}$, is the characteristic distance that particles travel for reaching steady state motion after being entrained by the stream. It is also referred to as the saturation or relaxation length [37]. In transient flows, this is the typical length for the sediment transport rate and particle activity to reach steady state. It is an input parameter in non-equilibrium sediment transport simulations [38, 39] and its parametric dependence remains unclear. Using dimensional analysis arguments, Charru [37] found that the adaptation length is inversely proportional to the particle velocity. More recently, Heyman et al. [7] included particle diffusion in the definition of $\ell_{c,d}$. We shall see that our theory is consistent with Heyman et al. [7] and recovers Charru [37]'s scaling in the absence of particle diffusion. The second theoretical issue addressed in the present paper concerns the formulation of a new relation for the steady-state particle activity or, equivalently, for the ratio between the erosion and deposition rates. Both rates are expressed in terms of a reference Shields number and reference sediment transport rate, as initially suggested by Buffington [29]. These expressions are of particular interest to situations in which the Shields number varies from incipient sediment motion to full mobility conditions. By bridging the gap between our formulation, existing bed-load transport theories [29, 30, 31] and scaling laws derived by Charru [37] and Lajeunesse et al. [40], we end up with new expressions for the erosion and deposition rates.

Next the applicability of the sdSVE formulation to real problems is illustrated with two examples. The first numerical benchmark we used has become a standard in numerical simulations with regards to erodible beds because of its practical interest. The reader is referred to previous numerical studies, e.g. [41, 38]. Here it serves to estimate the importance of particle diffusion relative to particle advection in sediment transport. The second numerical experiment illustrates the capability of the mean sdSVE equations to self-select the wavelength of anti-dunes when particle diffusion is included in the model. As far as we are aware, this is the first time that this remarkable feature is reported. This numerical experiment also shows that the convection and the diffusion transport rates ($\bar{q}_{c,s}$ and $\bar{q}_{d,s}$, respectively) are of comparable magnitude in the presence of bed forms.

The paper is organized as follows: the similarities and/or differences between the mean sdSVE equations, capacity (equilibrium) and non-capacity (non-equilibrium) formulations are summarized in § 2. The concept of *adaptation length* and its dependence on the particle diffusivity is revisited in Section 3, and the closure equations for the erosion/deposition rates are presented in Section 4. Next, Section 5 is devoted to numerical simulations of flume experiments. Accuracy and performance are evaluated by comparing numerical simulations with available theoretical solutions and experimental related to channel degradation and anti-dunes migration in gravel bed streams [11, 32, 33, 34, 35, 36]. Conclusions are finally presented in § 6.

2. Equivalence between sediment transport formulations

Two approaches can be used for simulating sediment transport: (i) the classical paradigm with a sediment transport rate defined as a conditional function of the Shields number $\bar{q}_s = \bar{q}_{ss}(Sh)$ ('conditional' because the Shield number must be in excess of a critical value for $\bar{q}_s$ to be nonzero), (ii) an alternative approach (originally developed by Einstein [42]) in which sediment transport results from the imbalance between the entrainment and deposition rates introduced in equations (6)-(7). An overview of the relevant literature and the relation with the sdSVE equations (1)-(4b) are presented in Section 2.1 for approach (i) and Sections 2.2–2.3 for approach (ii). A complete state of the art is beyond the scope of this paper and so we will essentially summarize the main ideas.

2.1. Uniform flow down sloping bed: steady state sediment transport rate

Let us consider an inclined bed with constant bottom slope $-\partial_x y_b = \tan\theta$. The solution to the Saint-Venant-Exner equations (1)-(3) and (4b) for a steady uniform flow ($\partial_x = \partial_t = 0$) is given by $h = H$, $\bar{v} = V$, $y_b = -x\tan\theta$, $\langle\gamma\rangle = \langle\gamma\rangle_{ss}$ and $E = D$, where H denotes the flow depth, V is the flow depth-averaged velocity and $\langle\gamma\rangle_{ss}$ is the steady-state particle activity. Given the water discharge per unit width $Q = H\,V$ and the bottom slope $\tan\theta$, the hydraulic variables H and V are obtained from the balance between the gravitational force and flow resistance on the right-hand side of the momentum balance equation (2). In nondimensional form, this relation reads

$$\tan\theta = \frac{f\,V^2}{8\,g\,H} = \frac{f}{8}\,Fr^2 \tag{8}$$

where $Fr = V/\sqrt{g\,H}$ denotes the Froude number. In general, the Darcy-Weisbach friction factor f is a nonlinear function of the relative grain roughness $\delta^2 = d/H$ [43] and so equation (8) is to be solved iteratively.

Working under the Shields paradigm [29], we assume that sediment is eroded and transported by the flow when the Shields number Sh is in excess of the critical value Sh_{cr} [43]. Shields used dimensional analysis to demonstrate that $\bar{q}_{ss} = \bar{q}_{ss}(Sh)$ [29]. Under steady-state plane-bed conditions, the Shields number depends on the bed slope $\tan\theta$ and relative roughness δ^2 [11]

$$Sh = \frac{\tau_b}{\rho\,(s-1)\,g\,d} = \frac{f\,Fr^2}{8\,(s-1)\,\delta^2} = \frac{\tan\theta}{(s-1)\,\delta^2}\,. \tag{9}$$

If sediment motion occurs, i.e., for $Sh > Sh_{cr}$, the steady-state particle activity $\langle\gamma\rangle_{ss}$ is calculated by considering the balance between the erosion and deposition rates, i.e., by solving $E = D$. Appropriate closure equations are therefore required. In the classical approach (i), a number of studies have found that the deposition and entrainment rates satisfy

$$D = \kappa\,\langle\gamma\rangle \text{ and } E = \lambda, \tag{10}$$

where λ is a constant independent of $\langle\gamma\rangle$ [41, 27, 28, 40, 37]. As a consequence, the steady-state particle activity is given by

$$\langle\gamma\rangle_{ss} = \frac{\lambda}{\kappa} \tag{11}$$

and the steady state sediment transport rate is

$$\bar{q}_{ss} = \bar{u}_s\,\langle\gamma\rangle_{ss} = \beta\,\bar{v}\,\frac{\lambda}{\kappa}\,, \tag{12}$$

where β denotes the sediment-to-liquid velocity ratio.

Contrasting with the Shields approach, Einstein [26]'s approach does not involve any threshold for sediment incipient motion (this is tantamount to setting $Sh_{cr} = 0$). Buffington [29], Cheng [30] and Wilcock and Crowe

[31] replaced the concept of critical Shields number Sh_{cr} with a *reference Shields number* Sh_* which is associated to the *reference bed load* $\bar{q}_{s*} = \epsilon$, usually $\epsilon \sim 10^{-4}$ m^2/s. These authors showed how experimental data can be scaled by introducing the *scaled sediment transport rate* $\hat{q}_{ss}(\hat{Sh}) = \bar{q}_{ss}(Sh)/\bar{q}_{ss}(Sh_*)$ where $\hat{Sh} = Sh/Sh_*$. In this way, the data collapse on a single 'master' curve independently of sediment properties.

Note that for the moment, we do not give any preference to one approach over the other. In Section 4, we will show how to switch from one formulation to the other.

Several steady-state bedload transport equations $\bar{q}_{ss}$ have been proposed and calibrated under nearly uniform flow conditions [20]. The results (11) and (12) inferred from the sdSVE equations are consistent with existing algebraic bedload transport equations provided that the λ-to-κ ratio satisfies

$$\frac{\lambda}{\kappa} = \frac{\bar{q}_{ss}(Sh)}{\bar{u}_s} = \frac{\bar{q}_{ss}(Sh)}{\beta\,\bar{v}}\,. \tag{13}$$

This condition is, however, poorly constrained as the dependence of λ and κ on Sh remains undecided for rapidly varying flows. For nearly uniform regimes and moderate Shields numbers ($Sh \approx 2\,Sh_{cr}$), Lajeunesse et al. [40] and Charru [37] obtained $\kappa = c_d\,V_s/d$, where $V_s = \sqrt{(s-1)\,g\,d}$ is the characteristic settling velocity and $c_d \approx 0.1$. Taking into account that sediment particles settle in steady water approximately at constant velocity V_s (we take $c_d = 1$ at $Sh = 0$), we expect that κ (or c_d) is a monotonically decreasing function of Sh. Indeed sediment deposition is negligible at sufficiently large Shields number because turbulence fluctuations are sufficiently strong to keep sediment in suspension [44]. For uniform and non-uniform sand mixtures, entrainment and deposition rates have been estimated by observing dune migration [45]. More accurate estimations of E and D would require high-resolution techniques such as particle tracking, but there are few data available [19]. We propose a method to calibrate κ and λ in Section 4 as they are essential to the model.

The bed load transport rate $\bar{q}_s$ reaches its steady state value $\bar{q}_{ss}(Sh)$ under steady uniform flow conditions, i.e., when $\partial_x \bar{q}_s = \partial_t \langle\gamma\rangle = 0$, so $E = D$, according to the mass balance condition (7), and there is no aggradation or degradation of the bed, i.e., $\partial_t y_b = 0$. Contrasting with this physical picture, approach (i) does not go into detail and so the relation $\bar{q}_s = \bar{q}_{ss}(Sh)$ is assumed to hold also under nonuniform flow conditions. The Exner equation (3) is thus defined as

$$(1-\zeta_b)\frac{\partial y_b}{\partial t} = \frac{\partial \bar{q}_{ss}}{\partial x}\,. \tag{14}$$

Formally this approximation holds under slowly varying flow conditions (when $\partial_t\langle\gamma\rangle \ll \lambda$) and in the absence of strong gradient of the sediment transport rate ($\partial_x \bar{q}_{ss} \ll \lambda$).

2.2. Quasi-steady, non-diffusive sediment transport: Exner equation and flux relation equation

By setting $D_u = 0$, keeping only the first (algebraic) contribution in the definition (6) of the sediment transport rate (i.e. $\bar{q}_s = \bar{u}_s\langle\gamma\rangle$), neglecting the temporal variation $\partial_t\langle\gamma\rangle$, and substituting (4b) into (3), we end up with the standard version of Exner equation [46]:

$$(1-\zeta_b)\frac{\partial y_b}{\partial t} - \frac{\partial \bar{q}_s}{\partial x} = 0. \tag{15}$$

In this case, the bed load transport rate $\bar{q}_s$ is derived from equation (7). We thus obtain the *flux relaxation equation*:

$$\frac{\partial}{\partial x}(\beta\,\bar{v}\,\langle\gamma\rangle) = \lambda - \kappa\,\langle\gamma\rangle \quad \text{or} \quad \frac{\partial \bar{q}_s}{\partial x} = \frac{1}{\ell_c}\,(\bar{q}_s - \bar{q}_{ss})\ , \tag{16}$$

where the adaptation length is $\ell_c = \bar{u}_s/\kappa$.

In the limiting case $|\partial_x \bar{q}_s| \ll \lambda$, the leading-order solution to the flux relaxation equation (16) is $\langle\gamma\rangle = \langle\gamma\rangle_{ss}$ or $\bar{q}_s = \bar{q}_{ss}$, which shows that our formulation is consistent with the Exner equation based on the algebraic bed load transport equation $\bar{q}_{ss}$ (14). By defining the adaptation length as $\ell_c = \bar{u}_s/\kappa$, we also retrieve the flux relaxation equation obtained by Charru [37]. It is worth mentioning that the flux relaxation equation (16) allows for the formation of ripples with physically consistent wavelengths at subcritical Froude numbers [47] while the standard Exner equation does not (it is unconditionally stable at $Fr < 2$ [48]). Let us also mention that El Kadi Abderrezzak and Paquier [38] successfully computed several problems of practical relevance using (15)-(16), while more recently, Li and Qi [49] have built analytical solutions related to channel degradation under slowly varying flow conditions by using a constant adaptation length ℓ_c and in doing so, they have been able to reproduce Phillips and Sutherland [50]'s experiments. These examples illustrate the better performance of the formulation (16) (or equation (4b)) compared to the classical Exner equation (14). Let us move on to the unsteady case and comment on the similarities with non-equilibrium sediment transport equations.

2.3. Non-diffusive bed load transport: non-equilibrium, non-capacity or unsteady flux relaxation equation

In recent years, emphasis has been given to non-equilibrium sediment transport models, particularly in the numerical simulations of rapidly varying flows. These models now offer a credible alternative to the classical Exner approach. Some examples that provide evidence of the capabilities of this approach include the simulation of erodible dam-break flows [51, 52, 39], aggradation due to overloading, and degradation by overtopping flow [41, 52]. The underlying idea is that sediment transport results from the imbalance between erosion and entrainment. It has been used in various settings: bed load transport [26, 53], turbidity currents [54] , suspended sediment transport in rivers [55], and total sediment load [56].

The mathematical similarity between the mean sdSVE equations and non-equilibrium bed load transport equations is readily observed by neglecting sediment diffusion (i.e., by setting $D_u = 0$) and using the definition of the local bed load transport equation $\bar{q}_s = \bar{u}_s\langle\gamma\rangle$, that allow us to recast equations (3) and (4b) in the following form

$$(1-\zeta_b)\frac{\partial y_b}{\partial t} = \frac{1}{\ell_c}\,(\bar{q}_{ss} - \bar{q}_s)\ , \tag{17}$$

$$\frac{\partial}{\partial t}\left(\frac{\bar{q}_s}{\bar{u}_s}\right) + \frac{\partial \bar{q}_s}{\partial x} = \frac{1}{\ell_c}\,(\bar{q}_s - \bar{q}_{ss})\ . \tag{18}$$

Relations (17)-(18) are similar to the non-equilibrium or non-capacity bed load equations (e.g., see Wu [27] and Zhang et al. [39]). Some authors prefer to express them in terms of an equivalent depth-averaged volumetric concentration of sediment [51, 28], while others keep the mean particle activity $\langle\gamma\rangle$ (instead of $\bar{q}_s$) as the unknown to be determined [47, 40]. Recall that we arrived at equation (18) by taking the ensemble average of the Langevin equation (4a) for the Poisson density b. We deduce that current sediment transport equations calculate the mean particle activity or mean sediment transport rate by ignoring particle diffusion. Sediment diffusion is, however, inherent to bed load transport [9, 10] as this happens to other random flight processes [1, 2]. So sediment diffusion and its part played in sediment transport deserve further numerical studies, which has motivated the work presented in the next section.

3. The adaptation length

We have seen in the introduction that the adaptation length is the characteristic distance travelled by particles for reaching steady state motion; the sediment transport rate and particle activity also come close to their steady state values $\bar{q}_{ss}$ and $\langle\gamma\rangle_{ss}$, respectively. Heyman et al. [7] have recently derived the expression of the adaptation length by calculating the steady-state solution to the scalar transport equation (4b) for a prescribed uniform particle velocity $\bar{u}_s$ and the following boundary conditions:

$$\begin{aligned} &\frac{d}{\partial x}(\bar{u}_s\,\langle\gamma\rangle) - \frac{d^2}{\partial x^2}(D_u\langle\gamma\rangle) = \lambda - \kappa\,\langle\gamma\rangle\,, \\ &\langle\gamma\rangle = 0 \text{ at } x = 0 \quad \text{and} \quad \frac{d\langle\gamma\rangle}{dx} = 0 \text{ at } x \to \infty\,. \end{aligned} \tag{19}$$

Solving equation (19) for $\langle\gamma\rangle$ (and assuming a constant sediment velocity $\bar{u}_s$), we get

$$\frac{\langle\gamma\rangle(x)}{\langle\gamma\rangle_{ss}} = 1 - \exp^{-x/\ell_{c,d}} \quad \text{with} \quad \ell_{c,d} = \frac{2\,D_u}{\bar{u}_s}\left[\sqrt{1 + 4\,\frac{D_u\,\kappa}{\bar{u}_s^2}} - 1\right]^{-1}. \tag{20}$$

The exact solution (20) is marked up with a solid line in Fig. 1. At the upstream boundary, the particle activity vanishes owing to the prescribed Dirichlet boundary condition $\langle\gamma\rangle = 0$ at $x = 0$. Assuming that particles travel downward (in the streamwise direction, i.e. $\bar{u}_s > 0$), the particle activity increases monotically along the x axis. Far away from the inlet (i.e. for $x \gg \ell_{c,d}$), the particle activity reaches its steady state value $\langle\gamma\rangle = \langle\gamma\rangle_{ss}$. To give an example, we provide the numerical values of $\langle\gamma\rangle$ at points $x/\ell_{c,d} = 1$, 2.3 and 4.6: equation (20) yields $\langle\gamma\rangle/\langle\gamma\rangle_{ss} = 0.63$, 0.90 and 0.99, respectively. In practice, steady state is observed for distances in excess of $4\,\ell_{c,d}$. Note that particle diffusion does not affect the steady-state particle activity $\langle\gamma\rangle_{ss} = \lambda/\kappa = \bar{q}_{ss}/\bar{u}_s$. It is also worth highlighting that the adaptation length does not depend explicitly on the erosion rate λ. At leading order, $\ell_{c,d}$ is expected to reflect the balance between particle convective and deposition [37]. The Taylor series expansion at $D_u = 0$

$$\ell_{c,d} = \ell_c + \ell_d\left[\frac{\ell_d}{\ell_c} - \left(\frac{\ell_d}{\ell_c}\right)^3 + 2\left(\frac{\ell_d}{\ell_c}\right)^5 + O\left(\left(\frac{\ell_d}{\ell_c}\right)^7\right)\right], \quad \ell_c = \frac{\bar{u}_s}{\kappa}, \quad \ell_d = \sqrt{\frac{D_u}{\kappa}}. \tag{21}$$

shows that $\ell_{c,d} \approx \ell_c$ in the limit of $\ell_d \to 0$. How sediment diffusion affects the adaptation length (relative to particle advection) can be evaluated using the ratio $\ell_d/\ell_c = Pe^{-1} = (D_u\,\kappa/\bar{u}_s^2)^{1/2}$ which represents the inverse of the Péclet number [10]. For $Pe \gg 1$ (i.e. $D_u\,\kappa \ll u_s^2$), particle advection is the predominant mechanism, whereas for $Pe \to 0$, sediment diffusion is the key process.

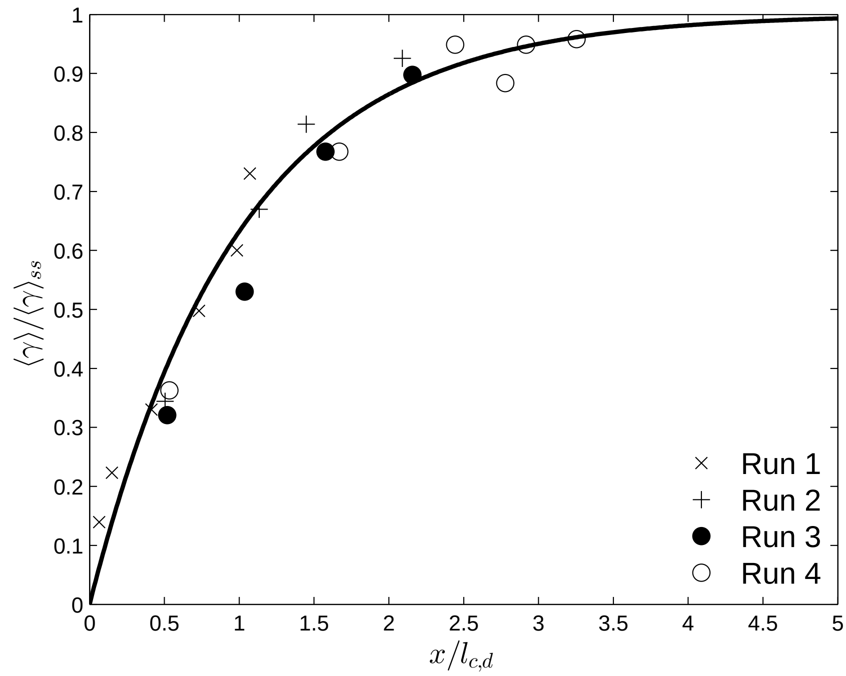

Figure 1: Nondimensional particle activity $\langle\gamma\rangle/\langle\gamma\rangle_{ss}$ at several scaled distances $x/\ell_{c,d}$ in the experiments carried out by Jain [60] (Run 1 and Run 2) and Bagnold [61] (Run 3 and Run 4). The solid line represents the theoretical solution (20). The adaptation length $\ell_{c,d}$ was calibrated by fitting the dimensional solution $\langle\gamma\rangle(x)$ to each experimental series. This yields: 17.67, 6.35, 1.96 and 0.47 m for transport stage parameters $T = Sh/Sh_{cr} - 1$ of [60] 0.24, 0.62, 1.68 and 16.6 from Run 1 to Run 4, respectively.

There is growing experimental evidence of the part played by particle diffusion under weak and partial bed load transport, e.g., see Nikora et al. [3] and Heyman et al. [7]. Taking a theoretical perspective, Furbish et al. [9] and Ancey and Heyman [10] showed that particle diffusion is one of the key processes that control particle activity fluctuations. There are different methods for evaluating particle diffusivity. Analyses of particle trajectories lead to values ranging from 0.04 m^2/s [57] to 50 m^2/s [7]. These values are much higher than water turbulent diffusivity, approximately $D_u \approx 0.3\, H\, V\, \sqrt{f/8} \sim O(10^{-3})$ m^2/s under uniform flow conditions [2]. Other techniques based on the spread of particle samples also lead to smaller values, e.g. 4.6 cm^2/s in Drake et al. [58] and $2.67 - 4.14$ cm^2/s in Ramos et al. [59].

Diffusion in the advection diffusion equation (4b) arises from the ensemble average of the Langevin equation (4a), similarly to what is obtained with Lagrangian models of turbulent particle suspensions [2]. As a possible stochastic model underpinning non-equilibrium bed load transport equations is the Langevin equation (4a) (see Section 2.3), we think that numerical results can be made more realistic by including equation (4a) into the set of governing equations. In doing so, we do not need to prescribe the adaptation length $\ell_{c,d}$ as it is calculated in the course of computations. This is the first step towards numerical stochastic simulation of bed load transport using the Langevin equation (4a) (see by Bohorquez and Ancey [11] for further information).

To evaluate the parametric dependence of the adaptation length $\ell_{c,d}$, we shall use the experimental data obtained by Jain [60] (hydraulic erosion) and Bagnold [61] (aeolian erosion). We have calibrated $\ell_{c,d}$ by fitting the theoretical solution (20) to their experimental results. Figure 1 shows the streamwise variation in the nondimensional particle activity $\langle\gamma\rangle(x)/\langle\gamma\rangle_{ss}$ as a function of the non-dimensional coordinate $x/\ell_{c,d}$. A summary of the experimental conditions can be found in the figure caption. Note that the data samples of the four experimental runs closely match the theoretical solution (20). The adaptation length decreases with increasing Shields numbers Sh (or transport stage parameters $T = Sh/Sh_{cr} - 1$). Furthermore, the steady-state sediment transport rate $\bar{q}_{ss}$ increases with T. In particular we obtained $\ell_{c,d} = \{17.67, 6.35, 1.96, 0.47\}$ m and $\bar{q}_{ss} = \{2.2, 19.0, 10.0, 148.0\}$ g/s/m for $T = \{0.24, 0.62, 1.68, 16.6\}$. This means that the ratio $\bar{q}_{ss}/\ell_{c,d}$ grows monotically when the flow passes from the partial- to the full-mobility regimes. Consequently, the local bed load transport rate $\bar{q}_s$ and the local particle activity $\langle\gamma\rangle$ tend to the steady state values $\bar{q}_{ss}$ and $\langle\gamma\rangle_{ss}$ when $Sh \gg Sh_{cr}$. This may explain why steady-state sediment transport theories perform well for the full mobility regime (see, e.g., García [20]). In contrast, non-equilibrium sediment transport theories are required when the flow conditions are close to the threshold of erosion onset, typically for $Sh/Sh_{cr} < 2$. Mathematically the right-hand side of equations (16)-(18), which scales as $\bar{q}_{ss}/\ell_{c,d}$, is much more important than the other terms, allowing us to set $\bar{q}_s \approx \bar{q}_{ss}$ when $Sh \gg Sh_{cr}$. With regards to the $\langle\gamma\rangle$-equation (19), it readily follows that the entrainment rate λ is key to sediment dynamics for flow conditions that are far from the threshold of incipient motion and, consequently, the left-hand side of equation (19) becomes negligible. This is equivalent to setting $\langle\gamma\rangle \approx \langle\gamma\rangle_{ss} = \lambda/\kappa$ and $\ell_{c,d} \to 0$ for $Sh \gg Sh_{cr}$. This finding corroborates the experimental evidence that particle diffusion is significant mostly under weak and partial bed load transport.

We conclude this section by pointing out that Bohorquez and Ancey [11] have shown that the diffusive term competes with the advection, erosion and deposition of sediment particles under the partial mobility regime. It plays a key role in the development of bed forms and is pivotal in the self-selection mechanism of the bed form wavelength

$$\frac{\bar{u}_s\,\langle\gamma\rangle_{ss}}{\lambda\,\ell_{c,d}} \sim \frac{D_u\,\langle\gamma\rangle_{ss}}{\lambda\,\ell_{c,d}^2} \sim 1 \quad \text{with } Sh/Sh_{cr} \sim O(1). \tag{22}$$

The adaptation length $\ell_{c,d}$ is, however, independent of the bedform wavelength Λ, which is mostly controlled by the eddy diffusivity ν—introduced in the momentum balance equation (2)—of the water phase and particle diffusivity D_u of the sediment phase. We wish to emphasize this point because on many occasions, both concepts are mixed (which is tantamount to setting $\ell_{c,d} \approx \Lambda$). We refer the reader to [11] and Section 5.2 for detail on the influence of D_u and ν on the selection of the wavelength Λ.

4. The steady-state sediment transport rate and particle activity

In this section we revisit the closure equation for the steady-state particle activity $\langle\gamma\rangle_{ss}$ (11), which fixes the value of the λ/κ ratio. As our objective is to build a theoretical framework consistent with the steady state sediment transport formulation, we first consider equation (13), which relates $\langle\gamma\rangle_{ss}$ to the steady-state sediment transport rate $\bar{q}_{ss}$. A similar approach was adopted in [11], where we used Fernandez Luque and van Beek [62]'s formula for evaluating the bed load transport rate in the full mobility regime, which allowed us to write

$$\bar{q}_{ss} = \langle\gamma\rangle_{ss}\,\bar{u}_s \quad \text{with} \quad \langle\gamma\rangle_{ss} = \frac{\lambda}{\kappa} = \frac{c_e\,V_p}{c_d\,d^2}\,(Sh - Sh_{cr})\,, \quad \bar{u}_s = \beta\,\bar{v}\,, \quad Sh \gg Sh_{cr} \tag{23}$$

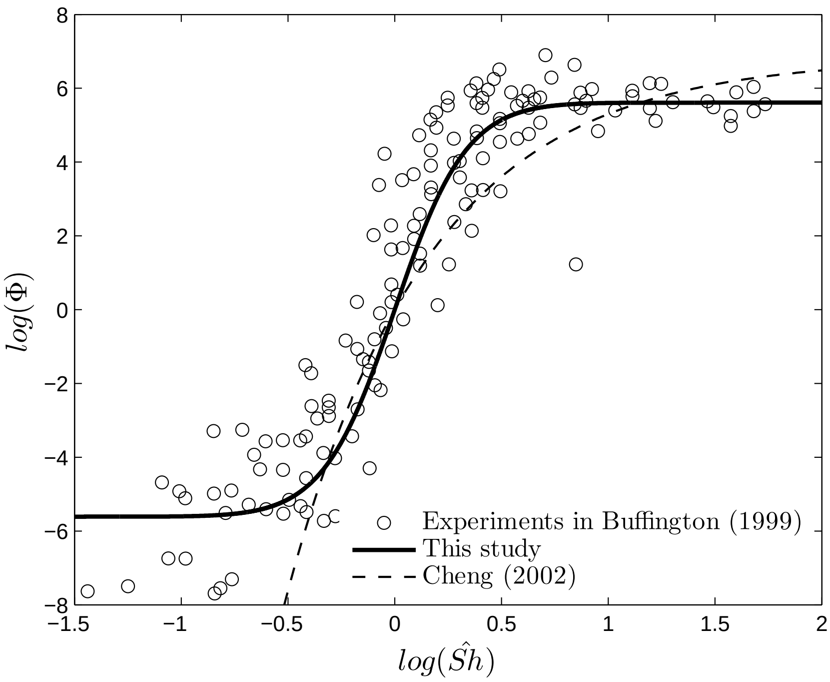

Figure 2: Comparison between the scaling factor $\Phi(\hat{Sh})$ given by (25), the experimental data collected by Buffington [29] and Cheng [30] equation.

in which $c_e/c_d = 1.75$ [62, 40] and the sediment-to-water velocity function $\beta \leq 1$ depends on the Darcy-Weisbach friction factor f and the nondimensional grain size $d_* = (d^3\,(s-1)\,g/\nu)^{1/3}$ or any combination of parameters that represent the particle size and the turbulent boundary layer characteristics at the bed bottom, e.g., see Yalin and da Silva [63]. Equation (23) is equivalent to Bagnold [64]'s formula; Yalin and da Silva [63] stated that "it is preferred because it is simple, it is accurate as any, and it reflects clearly the meaning of the bed load rate". Most existing algebraic expressions of $\bar{q}_{ss}$ exhibit a similar scaling as (23): $\bar{q}_{ss} \propto Sh^{3/2}$ for $Sh \gg Sh_{cr}$ (e.g., see García [20] and Julien [43]), but it should be remembered that these are not accurate when $Sh \to Sh_{cr}$ since $\bar{q}_{ss} \propto Sh^{17.5}$ empirically (e.g., see Buffington [29]).

In order to extend the range of applicability of our model to the partial- and full-mobility regimes, we propose a new calibration that involves two reference constants $\{Sh_*, \bar{q}_{s*}\}$ (they only depend on the sediment properties, essentially d_* [30, 31]). Within this framework, determining the reference bedload transport rate value $\bar{q}_{s*}(d_*)$ at a given Shields number $Sh_*(d_*)$ makes it possible to apply the model for $Sh \geq 0$. In that case, the critical Shields number for the onset of sediment motion is set to $Sh_{cr} = 0$. By so doing, we retrieve the same parametric dependence as Fernandez Luque and van Beek [62] (among others) in the full mobility regime. By defining $\bar{q}_{ss}$ in equation (13) as

$$\bar{q}_{ss}(Sh) = \frac{\bar{q}_{s*}\, Sh^{3/2}}{Sh_*^{3/2}}\, \Phi\left(\frac{Sh}{Sh_*}\right), \tag{24}$$

we can fit the experimental data collected by Buffington [29] in the plane $\{\hat{Sh}, \hat{q}_{ss}/\hat{Sh}^{3/2}\}$ with the following equation (see Fig. 2):

$$\log(\Phi) = 5.61 - 11.22 \left[1 + \exp^{-37.41 \log(\hat{Sh})/(\log(\hat{Sh})^2 - 6.22)}\right]^{-1}, \tag{25}$$

where $\hat{q}_{ss} = \bar{q}_{ss}/\bar{q}_{s*}$ is the scaled bed load function and $\hat{Sh} = Sh/Sh_*$ is the scaled Shields number.

It is readily observed that the function Φ (25) tends to the constant value 273.14 when $Sh/Sh_* > 2.72$, i.e. $\log(\Phi) = 5.61$ if $\log(\hat{Sh}) > 1$. Consequently, equation (24) ensures that $\bar{q}_{ss} \propto Sh^{3/2}$ in the full mobility regime because Φ is constant in equation (25). For $0.5 < Sh/Sh_* < 2$, the function Φ increases rapidly when increasing Sh and it closely describes the experimental trend. Cheng [30] proposed the exponential function $\bar{q}_{ss}/(V_s\, d) = 13\, Sh^{3/2} \exp(-0.05\, Sh^{-3/2})$ that has also been plotted in Fig. 2 with $\bar{q}_{s*}/(V_s\, d) = 10^{-4}$ together with the data collected by Buffington [29] and equation (25). Both functions satisfy the property $\Phi = 1$ when $Sh = Sh_*$ and thus $\bar{q}_{ss} = \bar{q}_{s*}$ at the reference Shields number. A slight difference between the two approximations lies in the regularization of the function (25) at the lowest sediment transport rates, for which $\Phi \approx 0.0037$. At these low Shields numbers, the experimental data are very noisy and the solid transport rate fluctuations exceed the mean values, which is a further motivation for using a stochastic framework [10]. In our opinion, a strength of the non-equilibrium bed load approach is that it can be readily be incorporated in this stochastic framework. Further information can be found in [11].

The next step is to derive the steady state particle activity $\langle\gamma\rangle_{ss}$ from $\bar{q}_{ss}$. Substituting equation (24) into equation (13) and using $\bar{v} = \sqrt{8/f}\, V_s\, Sh^{1/2}$, we end up with

$$\langle\gamma\rangle_{ss} = \frac{\lambda}{\kappa} = \langle\gamma\rangle_* \, \hat{Sh}\, \Phi(\hat{Sh}), \quad \langle\gamma\rangle_* = \frac{\bar{q}_{s*}\sqrt{f}}{\beta\, V_s \sqrt{8\, Sh_*}}. \tag{26}$$

At the reference level we get $\hat{Sh} = 1$, $\Phi = 1$ and $\langle\gamma\rangle_{ss} = \langle\gamma\rangle_*$. The sediment-to-water velocity ratio β depends on the friction factor as $\beta \propto f^{1/2}$ [11] and so, in (26), $\langle\gamma\rangle_*$ is independent of the flow conditions. At large Shields number, we recover the scaling relation $\langle\gamma\rangle_{ss} \propto Sh$ (23) as Fernandez Luque and van Beek [62], Charru [37] and Lajeunesse et al. [40] also found. In contrast, at low Shields number, the function Φ plays a non-negligible role. Indeed, identifying $\langle\gamma\rangle_{ss}$ in equations (23) and (26), we end up with

$$\frac{c_e}{c_d} = \frac{\langle\gamma\rangle_*\, d^2}{Sh_*\, V_p}\, \Phi(\hat{Sh}). \tag{27}$$

Lajeunesse et al. [40] calibrated the parameters c_e and c_d by tracking the motion of individual grains in well-controlled flume experiments. They found $c_e/c_d = 1.75$ and $c_d = 0.094 \pm 0.006$ at moderate/high Shields number. Similarly, our expression (27) yields a constant ratio c_e/c_d at $Sh \gg Sh_*$ where $\Phi = 1$. Note that for weak sediment transport, this ratio is no longer constant, but depends on $\hat{Sh}$. So the calibrated formula $\Phi(\hat{Sh})$ (25) can be used together with equation (26) to evaluate equation (27) at any Shields number. Alternatively, the former closure equation (23) could be used in the numerical simulation of partial/intense bed load transport with a preliminary calibration of the parameters c_e and c_d that is equivalent to including the scaling factor Φ (see example in Section (5.1)).

5. Numerical simulation of flume experiment

We present two numerical experiments in order to benchmark the numerical results against experimental and theoretical solutions: Section 5.1 is devoted to the simulation of the degradation of a sloping channel (Test 3 in Newton [32]'s experiment); then, in Section 5.2, a numerical study of anti-dunes migration in gravel bed streams over steep slopes is presented [33, 34, 35, 36]. We follow the same strategy as in our previous work to discretize and integrate the ensemble-averaged sdSVE equations numerically. A fractional-step method was applied to split the advection-diffusion equations (1)-(4b) into a hyperbolic subproblem with source terms and a parabolic subproblem. The hyperbolic subproblem was solved numerically with a fifth-order accurate, weighted essentially nonoscillatory (WENO) scheme, second-order-accurate, source term discretization and third-order accurate, strong stability-preserving (SSP), Runge-Kutta time integration—denoted by SSPRK(3,3) in Gottlieb et al. [65]. The eddy and particle diffusivity terms were integrated with the one-step implicit Crank-Nicholson scheme, which is second-order accurate in space and time. Specific details of the numerical scheme and its implementation into the high-order finite volume library SharpClaw can be found in [11, 66].

5.1. Newton's degradation experiment

Newton [32] ran experiments on bed load transport in a flume including a 9.14 m long, 0.3 m wide 0.6 m deep test reach. A hopper filled with sand ($d = 0.69$ mm) fed the flume with sediment upstream of the test reach to ensure initial bed equilibrium along the flume. The bed load transport rate was maintained at equilibrium ($\bar{q}_s = \bar{q}_{ss}$) by recirculating sediment from the outlet to the inlet. Sediment supply was suddenly stopped to study bed degradation. The water discharge $Q = 0.0057$ m^3/s was kept constant during the experiment that lasted for 27 hours. Newton [32] monitored the bed load flux at the outlet of the flume, the thalweg elevation along the test reach at several points over time (1, 2.17, 4, 12 and 27 hr) and the evolution of the local scour depth at $x = 3.66$ m. The data in the downstream reach of the flume ($x > 6$ m) were used for calibration of the model parameters under steady state conditions, as described in section Appendix A. The rest of data was used for testing the numerical results shown in Fig. 3. Initially the bed was flat, inclined at the angle of 0.348° with respect to the horizontal, the bed porosity was $\zeta_b = 0.396$ and the depth-averaged velocity was $V = 0.47$ m/s. The flow regime was subcritical with the Froude number $Fr = 0.75$ at $t = 0$. The (fitted) non-dimensional parameters in the erosion-deposition model were $c_e = 8.4 \times 10^{-4}$ and $c_d = 1.6 \times 10^{-3}$, which leads to the following entrainment and deposition rates $\lambda = 4.65 \times 10^{-5}\,(Sh - Sh_{cr})\ \mathrm{m\,s^{-1}}$ and $\kappa = 0.245\ \mathrm{s^{-1}}$, respectively, with $Sh_{cr} = 0.044$. The sediment velocity $\bar{u}_s$ and the friction factor f were evaluated from equations (A.2)–(A.1). In the numerical simulations, the eddy viscosity was roughly estimated by $\nu \approx \nu_t\, h\, \bar{v}\sqrt{f/8}$ with $\nu_t = 4$ [11], the length of the computational was 8.6 m and the grid size consisted of 100 cells.

Table 1 summarises the boundary conditions employed in the numerical simulations. As the flow was subcritical during the experiment, the physical boundary conditions imposed for the hydraulic variables were the constant water discharge Q at the inlet and the outflow water depth $h_{out}(t)$ (see Fig. A.9(b)). Two additional numerical boundary conditions are required by the shallow water equations. We followed the most common approach by extrapolating the water depth from the inner computational domain to the ghost cells at the flume

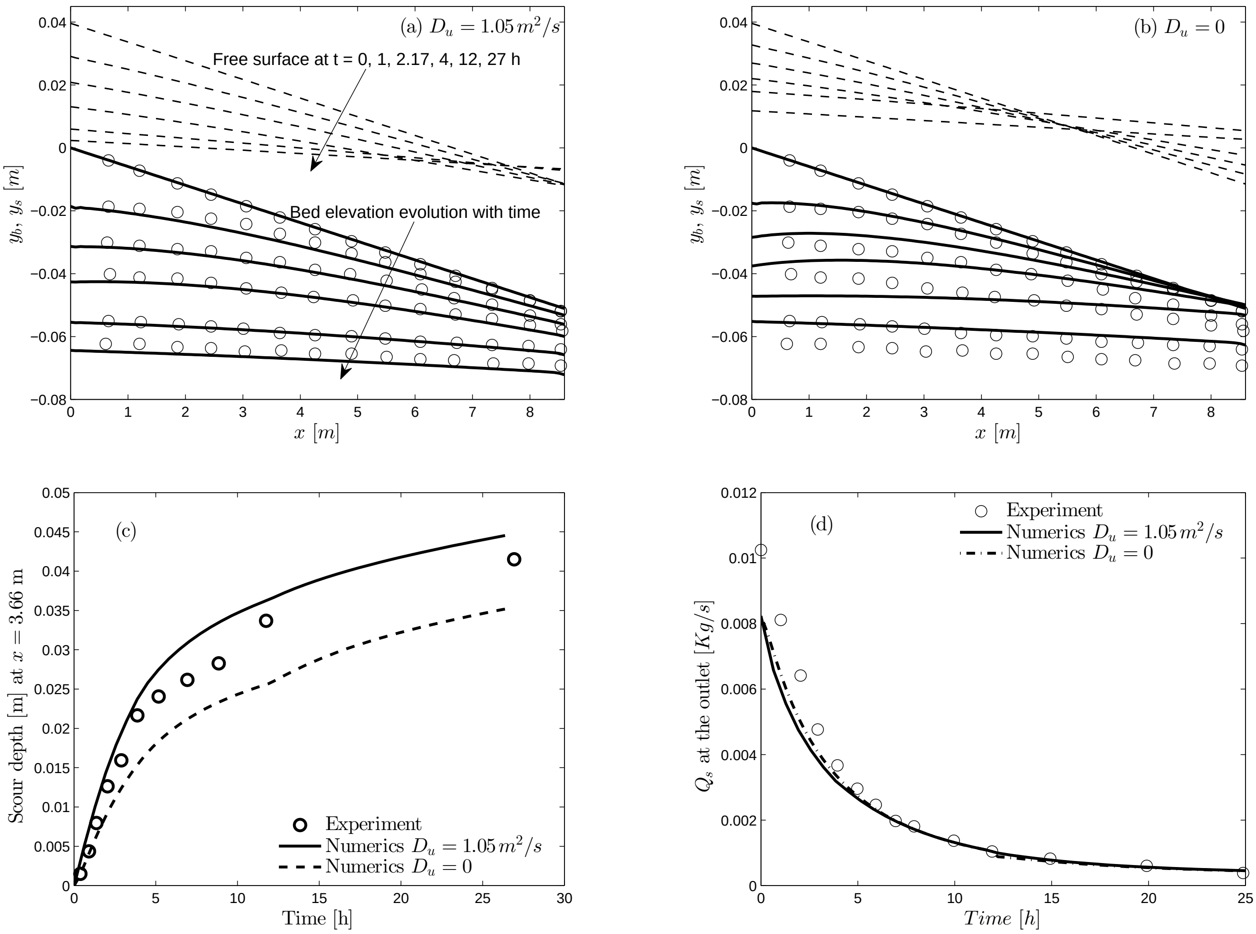

Figure 3: Time variation in the bed (solid line) and free-surface (dashed line) elevations for the diffusive (a) and non-diffusive (b) cases when simulating Test 3 run by Newton [32]. (c) Local depth scour at $x = 3.66$ m. (d) Sediment transport rate at the flume outlet. The symbols (circles) correspond to the experimental results [32].

inlet and the outgoing Riemann invariant at the flume outlet as described by Blayo and Debreu [67]. The absence of local scour in Newton's experiments is a clear evidence that sediment was entrained from the sand reservoir into the test reach because in the absence of sediment supply, degradation usually develops deep scour holes near the flume inlet, e.g., see Phillips and Sutherland [50]. In the absence of experimental detail, we performed an optimization process varying the value of $\partial_x\langle\gamma\rangle$ that was imposed at the inlet. This procedure was repeated by varying the particle diffusivity from 10^{-4} to 100 m^2/s. The optimum values that minimize the root mean square error in the thalweg elevation y_b (see Fig. 3(a)) is given in Table 1 for $D_u = 1.05$ m^2/s.

Table 1: Set of boundary conditions used in the numerical simulations. Physical and numerical boundary conditions are imposed depending on the subcritical or supercritical flow regime as explained in the main text.

Channel degradation		Anti-dunes migration	
Inlet	Outlet	Inlet	Outlet
$\partial_x h = 0$	$h = h_{out}(t)$	$h = H$	CVE
$\bar{v}\,h = Q/B$, $\partial_x\bar{v} = 0$	$\partial_x\left(\bar{v}\,h + 2\sqrt{g\,h}\right) = 0$	$\bar{v} = V$	CVE, $\partial_x\bar{v} = 0$
$\partial_x\langle\gamma\rangle = 11.6\,\langle\gamma\rangle\exp(-0.8\,t/3600)$	$\langle\gamma\rangle = \langle\gamma\rangle_{ss}$	$\langle\gamma\rangle = \langle\gamma\rangle_{ss}$	$\partial_x\langle\gamma\rangle = 0$
$\partial_x y_b = 0$	$\partial_x y_b = -f\,\bar{v}^2/8\,g\,h$	$\partial_x y_b = 0$	$\partial_x y_b = -f\,\bar{v}^2/8\,g\,h$

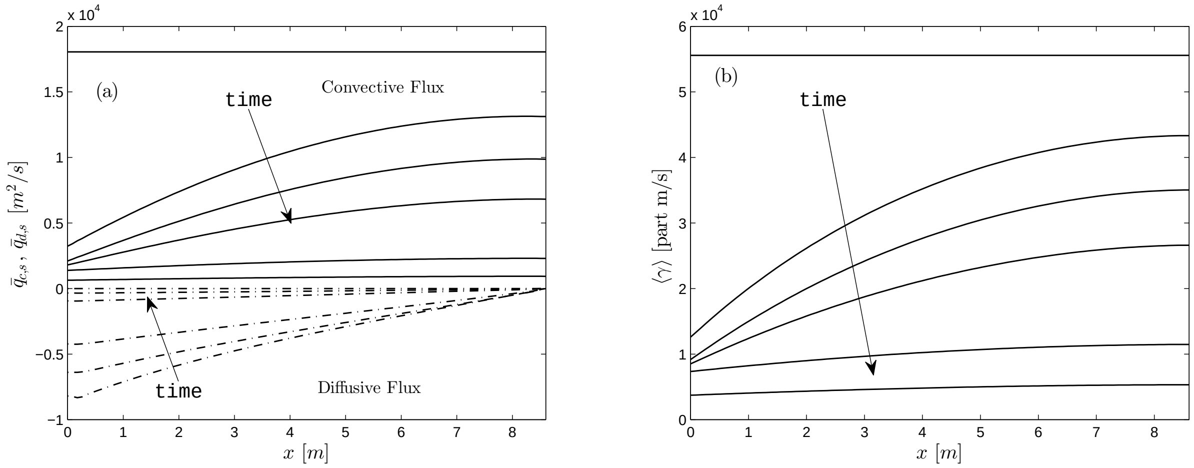

Figure 4: (a) Convective and diffusive sediment transport rates ($\bar{q}_{c,s}$ and $\bar{q}_{d,s}$, respectively) in Newton's experiments at the same times as in Fig. 3(a). Panel (b) shows the streamwise profiles of the mean particle activity $\langle\gamma\rangle(x)$. Note that the particle activity tends to the steady state value ($\langle\gamma\rangle = \langle\gamma\rangle_{ss}$) and that the diffusive sediment transport rate vanishes ($\bar{q}_{d,s} \approx 0$) near the end of the flume.

Finally, we fixed the steady state particle activity $\langle\gamma\rangle = \langle\gamma\rangle_{ss}$ at the flume outlet, which is physically consistent with a flume length (~ 10 m) much larger than the adaptation length ($\ell_{c,d} \sim 1$ m).

Figure 3(a) shows that the simulated bed elevation (solid line) obtained with $D_u > 0$ is in good agreement with the experiments (empty circles) at all times. The root mean square error of the thalweg elevation is of the order of the grain size d, which is negligible. We found out that the bed slope decreases progressively as degradation progresses until to it reaches a nearly steady state at late time. The slope of the free surface (dashed line) remains nearly parallel to the bed. The flow depth increases with decreasing bed slope. In the absence of sediment diffusion, see Fig. 3(b), a shallow scour hole develops near the inlet for $t \leq 12$ h and flattens at late time. On the whole, particle diffusivity increases the total sediment transport rate with respect to the steady state value. We could have anticipated this result by noting the order of magnitude of the adaptation lengths. For the calibrated parameters $\kappa = 0.245$ s^{-1}, $D_u = 1.05$ m^2/s, $\beta = 0.692$ and $\bar{v} = 0.47$ m/s, the adaptation length takes the value $\ell_{c,d} = 2.84$ m, which is comparable with the zero diffusion value $\ell_c = 1.32$ m and the zero advection value $\ell_d = 2.07$ m. This indicates that both particle advection and diffusion play a part in the numerical simulation. Indeed, the agreement between the simulation and the experiment is excellent (poor) at $t = 27$ h with $D_u = 1.05$ m^2/s ($D_u = 0$). When $D_u = 0$, the excavation is, however, too small at $x = 3.66$ m whereas for $D_u > 0$, the predicted scour depths match the experimental values (Fig. 3(c)). As expected, with regards to the sediment transport rate, the non-diffusive solution at the outlet nearly overlaps the diffusive solution, see Fig. 3(d), because the flume is long enough for a uniform regime to take place near the outlet. Both numerical solutions are close to the experimental measurements at this location. This could be better understood by taking a closer look at the convective and diffusive contributions to the bed load transport.

Numerical simulations allow us to evaluate the relative importance of the convective and diffusive sediment transport rates, which are plotted in Fig. 4(a) for the same times as in Fig. 3(a). The convective sediment transport rate $\bar{q}_{c,s} = \bar{u}_s\langle\gamma\rangle$ and the diffusive rate $\bar{q}_{d,s} = \partial_x D_u\langle\gamma\rangle$ are shown in solid and dashed lines, respectively.

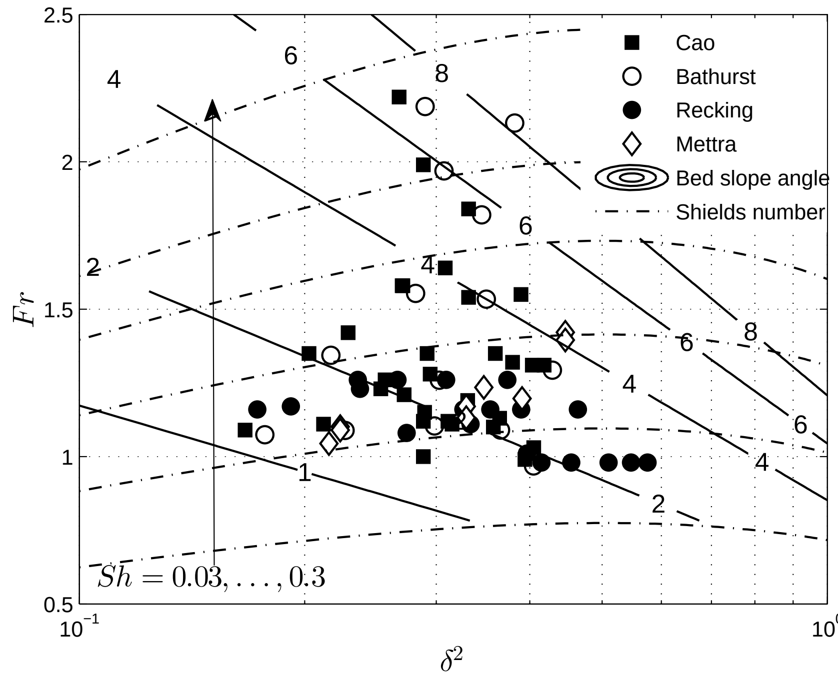

Figure 5: Diagram summarizing the flow conditions under which anti-dunes have been observed experimentally in gravel bed channels. The labelled solid lines represent constant bottom angles (in degrees) and the dotted-dashed lines represent the contour lines associated with a constant Shields number (Sh = 0.03, 0.06, 0.1, 0.15, 0.2, 0.3). The description of the experiments can be found in the original works by Cao [33], Bathurst et al. [34], Recking et al. [35] and Mettra [36]. Note that in gravel bed streams ($\delta^2 = d/H > 0.1$), anti-dunes occur typically for $1° \leq \theta \leq 4°$ in supercritical regime ($Fr > 1$).

The convective term $\bar{q}_{c,s}$ is positive as particles move downwards (in the streamwise direction). The diffusive sediment transport rate $\bar{q}_{d,s}$ is negative because the particle activity $\langle\gamma\rangle$ increases monotically from the flume inlet to the outlet, see Fig. 4(b). Since we have $\partial_x \bar{q}_{c,s} > 0$ and $\partial_x \bar{q}_{d,s} > 0$, both advection and diffusion contribute to eroding the bed. This explains why the water phase erodes more sediment in the diffusive case than in the non-diffusive case. Furthermore, non-equilibrium bed load transport develops mostly in the upstream reach of the flume and particles reach steady state motion after travelling a short distance (the equivalent of a few adaptation lengths). Near the flume outlet, sediment is in a steady state regime with $\langle\gamma\rangle \approx \langle\gamma\rangle_{ss}$. This explains why $\bar{q}_{d,s} \approx 0$ and why we observe the same values of sediment transport rate in Fig. 3(d), near the flume outlet in both simulations (this good agreement substantiates the assumptions used in the calibration stage).

5.2. Anti-dunes developments in gravel bed stream

One-dimensional shallow water flows over erodible steep slopes develop upstream migrating anti-dunes for Shields numbers in excess of the threshold for incipient sediment motion. Figure 5 summarizes the experimental conditions under which anti-dunes have been observed in gravel bed flumes. The flow regime is typically supercritical ($Fr > 1$), the flow depth is low relative to the grain size ($H < 10\,d$) and the bed is considered steep according to geomorphological criteria ($\theta > 1°$) [68], but the mean slope is shallow in the mathematical sense (i.e., $\cos\theta \approx 1$) with the important consequence that the pressure distribution (across the depth) is hydrostatic

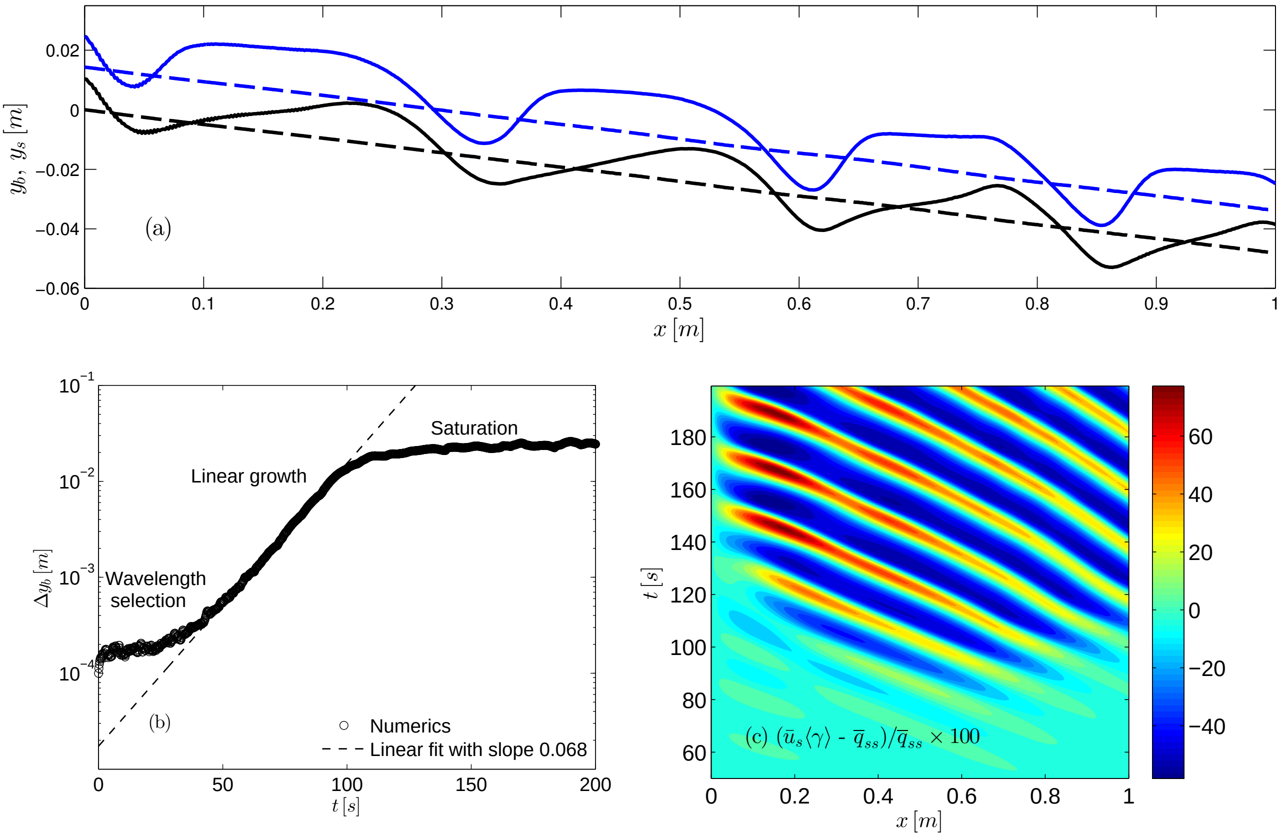

Figure 6: (a) Snapshots of the bed and free-surface elevations together at $t = 0$ and at $t = 200$ s: the dashed lines show the uniform base flow at $t = 0$ and solid lines show the anti-dunes train in the numerical simulation at $t = 200$ s. The blue (black, respectively) line corresponds to the free surface (bed elevation, respectively). (b) Evolution of the maximum perturbation in the bed elevation. (c) Convective contribution to the bed load transport rate in the plane $\{x, t\}$ scaled by the uniform background flow's steady-state transport rate $\bar{q}_{ss} = 86.49$ m^2/s.

and the Saint-Venant equations (1)-(2) are well-suited.

In gravel bed streams, anti-dune growth arises from an instability of the initial plane bed in uniform, steady flow. The instability mechanism was originally explained by Kennedy [14] using linear stability analysis of two-dimensional irrotational flows above erodible beds. More sophisticated linear stability theories using rotational flow equations for the water phase have been proposed by Colombini [69]. On the one hand, the computational cost of these alternatives is heavy because they need to solve for the vertical velocity component. On the other hand, the predictive capability of depth-averaged shallow water equations remains partial because they correspond to a non-rotational formulation (the vertical component of the velocity vector is neglected). When the Saint-Venant equations (1)-(2) are coupled with the Exner equation (14), the bed is unconditionally stable for $Fr < 2$ [48] and, consequently, the anti-dunes diagram 5 cannot be plotted. Here we show that the deterministic non-equilibrium formulation (1)-(4b) successfully captures anti-dune instability because of the existence of saddle points in the wavenumber space, which make the flow absolutely unstable. Furthermore this formulation catches the most unstable wavelength.

First we illustrate the development of upstream migrating anti-dunes when simulating the experimental conditions previously described (see Fig. 5). Second, the absolute nature of the instability is proven by the

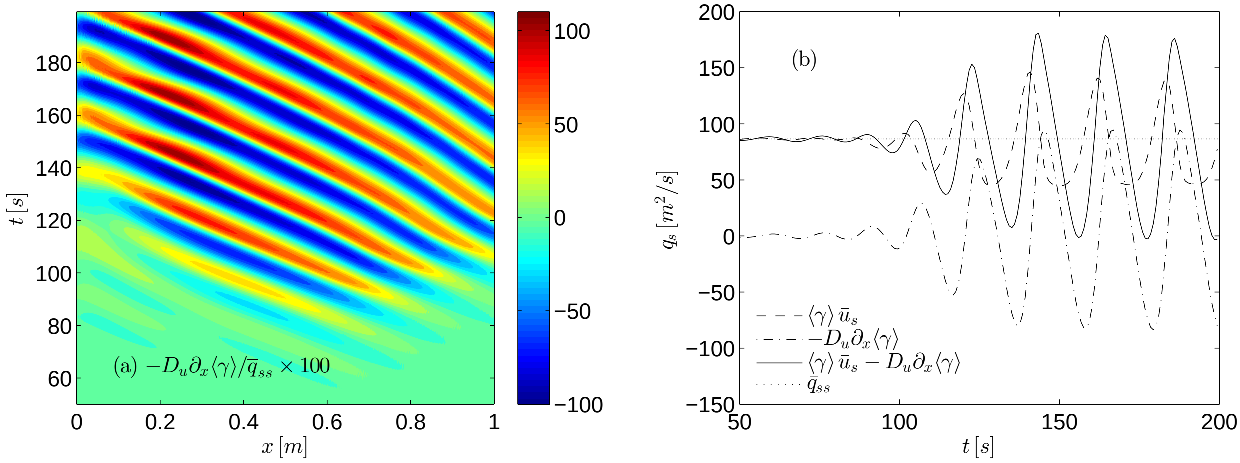

Figure 7: (a) Diffusion contribution to the sediment transport rate in the plane $\{x,t\}$ scaled by the uniform background flow's steady-state value $\bar{q}_{ss} = 86.49$ m^2/s. (b) Comparison between the diffusive (dotted-dashed line), convective (dashed line) and total (solid line) sediment transport rate with respect to the steady-state sediment transport $\bar{q}_{ss}$ (dotted line) at location $x = 0.24$ m.

existence of saddle points in the spatio-temporal stability analysis (e.g., see Schmid and Henningson [70] and Juniper et al. [71]), which allows us to predict the most unstable wavelength theoretically.

The simulated flow parameters correspond to the dimensionless numbers $Fr = 1.2$ and $\delta^2 = 0.4$ that come close to the experimental conditions imposed by Cao [33], Bathurst et al. [34], Recking et al. [35] and Mettra [36] in Fig. 5. Without loose of generality, we set the critical Shields number to $Sh_{cr} = 0.03$ for fine/medium gravels [29] while the Darcy-Weisbach friction factor f was evaluated from equation (A.1) with $k_s = 1$. The slope angle, Shields number and sediment-to-water velocity ratio associated with this set of values were computed from equations (8)-(9), which yields $\theta = 2.75°$, $Sh = 0.073$ ($Sh/Sh_{cr} > 2$) and $\beta = 1$ under uniform regime. Other model parameters were kept constant during the numerical simulation: $d = 5.74$ mm, $c_e = 0.1$, $c_d = 0.175$ ($\kappa = 5.31$ s^{-1}), $\zeta_b = 0.36$ and $D_u = 0.1$ m/s. Substituting these values into equation (23), we obtain the steady state bed load transport rate for the uniform base flow $\bar{q}_{ss} = 86.49$ m^2/s. This value will be used to establish the importance of sediment advection relative to diffusion in the presence of anti-dunes and non-uniform time-dependent flow conditions.

As in the previous simulations, the eddy viscosity was estimated at $\nu \approx \nu_t\, h\, \bar{v}\sqrt{f/8}$ with $\nu_t = 10$. The computational domain $0 \le x \le 1.5$ m was divided into 1000 cells. As the flow is supercritical at the inlet at any time during the numerical simulation, we imposed the boundary conditions summarized in Table 1. At the inlet, the water depth and flow depth-averaged velocity were fixed to $H = 0.0143$ m and $V = 0.45$ m/s, respectively, and the particle activity took its steady state value. At the outlet, the characteristic variable method (CVE) was employed for the three characteristic curves that travel outwards. In addition, a fairly good *sponge* layer was added in the outlet reach $x > 1$ m to ensure absorbing boundary conditions [72]. The initial conditions used in our computations were $h = H$, $\bar{v} = V$, $\langle\gamma\rangle = \langle\gamma\rangle_{ss}$ and $y_b = -x\,\tan\theta + \epsilon(x)$ where $\epsilon(x)$ is a random perturbation with amplitude 10^{-4} m. Below we report on the results in the reach $0 \le x \le 1$ m, which is not affected by the sponge layer.

Figure 6(a) shows the initial condition for the bed elevation (black dashed line) and water surface (blue

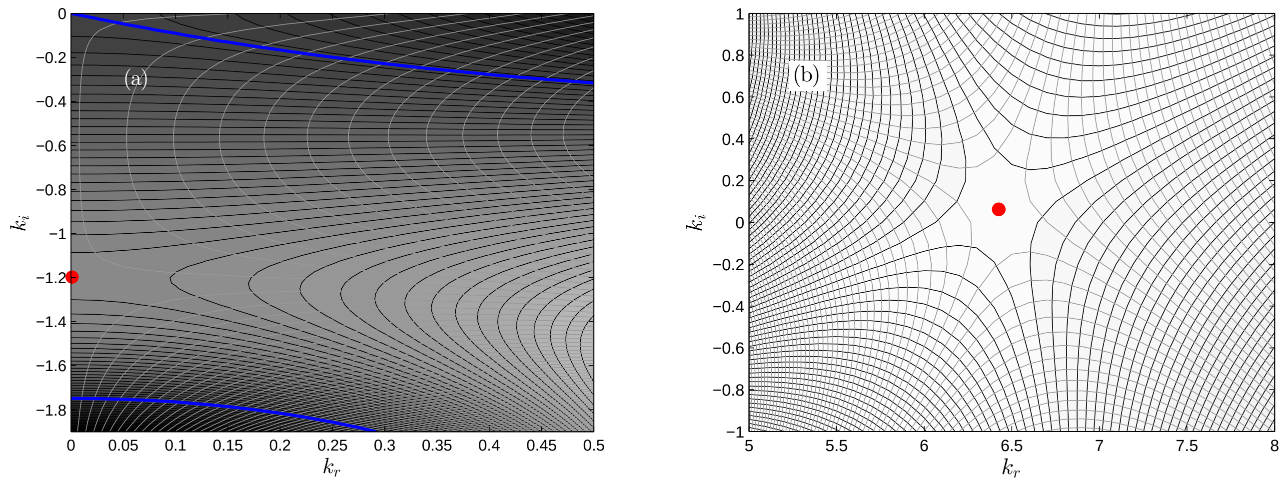

Figure 8: Red bullets show the pinch points location k_0 in the complex wavenumber plane $\{k_r, k_i\}$ using Briggs' method (isocontours of $\omega_r(k)$ and $\omega_i(k)$) for the parameter values in the numerical simulation of anti-dunes. The saddle points are pinched between branches k^+ (half-plane $k_i > 0$) and k^- (half-plane $k_i < 0$) issuing from distinct halves of the k-plane. Spatial branches $k^{\pm}(\omega)$ with $\omega_i = 0$ are coloured in blue.

dashed line). The initial perturbation introduced in the bed elevation cannot be observed because of its small amplitude. After a first stage in which the numerical solution self-selects a well-defined wavelength (for $t \leq 50$ s), the bed perturbation grows as $\Delta y_b(t) = \max(|y_b(x,t) - y_b(x,0)|) = \exp(0.068\,t)$ until time $t \approx 100$ s when the maximum amplitude of the bed perturbation saturates, see Fig. 6(b). The numerical solution at late time (solid lines) exhibits a train of anti-dunes with amplitudes as high as the initial water depth and similar wavelength $0.2 \leq \Lambda \leq 0.3$ m. The wavelength is slightly coarser upstream than downstream, which could be attributed to a nonlinear coarsening mechanism during the growth and propagation of the antidune from the reach outlet to the inlet. The water surface y_s and the bed elevation y_b are no longer plane as a result of bed form development. The free surface curvature is marked in the anti-dune's lee side while in the stoss side, the free surface remains nearly parallel to the initial bed. Obviously the flow velocity $\bar{v}$ and Shields number are non-uniform in the perturbed state, which induces spatio-temporal variations in the sediment transport rate $\bar{q}_s$.

The fluctuations of the sediment transport rate can be readily appreciated in Figs. 6(c)-7(a) where the convective and diffusive rates, $\bar{q}_{c,s}$ and $\bar{q}_{d,s}$, have been compared to the steady state bed transport rate $\bar{q}_{ss}$. The fluctuations of the convection transport rate is as high as $\pm 60\%$ of the steady state value. The diffusive transport rate is even higher, approximately $-\bar{q}_{ss} \leq \bar{q}_{d,s} \leq 1.1\,\bar{q}_{ss}$. The maximum deviation of the sediment transport rate from the steady state value is reached at $x \approx 0.24$ m. A detail of the evolution of each sediment transport component is shown in figure 7(b). The bed load transport rate exhibits marked up temporal fluctuations relative to its the mean value $\bar{q}_{ss}$ for $t \geq 150$ s, after the first transient stage. Note that the diffusive transport rate (dotted-dashed line) is as high as the steady state value (dotted line), which highlights the importance of particle diffusion in sediment transport. There is a lag time in the convective and diffusive transport rate fluctuations, but they do not counterbalance each other. Hence the total sediment transport also exhibits large fluctuations with a well defined frequency.

The spatial wavelength (and the temporal frequency) observed numerically in the nonlinear cycle at late time ($t \geq 150$ s) can be predicted using a spatio-temporal linear stability analysis. Hydrodynamic stability theory is well established and the reader is referred to the book by Schmid and Henningson [70] and the recent review by Juniper et al. [71] for further information. Here we follow the same steps as Bohorquez and Ancey [11]: first we define the nondimensional variables $z = y_b/H$, $\phi = \langle\gamma\rangle/\langle\gamma\rangle_{ss}$, $\eta = h/H$, $u = \bar{v}/V$, $\hat{x} = x \tan\theta/H$ and $\hat{t} = t\,V \tan\theta/H$; then, we linearise the nondimensional sdSVE equations around a uniform base flow by setting $(z, \phi, \eta, u) = (-\hat{x}, 1, 1, 1) + \epsilon\,(z', \phi', \eta', u')$ and retain only the terms of order $O(\epsilon)$, which leads to the linear perturbation equation; finally, we determine the saddle and cusp points of the eigenvalue problem. As the first and the second steps of these calculations are detailed in Sections 3.1-3.2 in [11], we do not repeat them here for the sake of brevity. So we focus on the determination of the saddle points.

The solution of the linear perturbation equations in the spatio-temporal stability analysis can be written as $(z', \phi', \eta', u') = \overline{T} \exp i(k\,\hat{x} - \omega\,\hat{t})$, where the eigenvector is denoted by $\overline{T} \equiv (\zeta, \Phi, \Gamma, U)^T$, the complex wavenumber by $k = k_r + i\,k_i$ and the complex frequency as $\omega = \omega_r + i\,\omega_i$. For the closure equations (23), the eigenvalues and eigenvectors are obtained from the following generalized eigenproblem $\overline{\overline{A}} \cdot \overline{T} = 0$:

$$\begin{aligned}&\left[-i\,\omega \begin{pmatrix} 1 & 0 & 0 \\ 0 & 1 & 0 \\ 0 & 0 & Fr^2 \end{pmatrix} + i\,k \begin{pmatrix} \beta & 0 & \beta \\ 0 & 1 & 1 \\ \frac{i\,k_e}{\omega} & 1 & Fr^2 - \frac{i\,2\,k_e}{\omega\,(1-u_*^2)} \end{pmatrix} - \right. \\ &\left. k^2 \begin{pmatrix} -\mathcal{D} & 0 & 0 \\ 0 & 0 & 0 \\ 0 & 0 & -\mathcal{V} \end{pmatrix} + \begin{pmatrix} k_d & 0 & -\frac{2\,k_d}{1-u_*^2} \\ 0 & 0 & 0 \\ 0 & -1 & 2 \end{pmatrix} \right] \cdot \begin{bmatrix} \Phi \\ \Gamma \\ V \end{bmatrix} = 0\,. \end{aligned} \tag{28}$$

The dimension of matrix (28) was reduced by one using $\zeta = i\,k_e\,\Phi/\omega - i\,2\,k_e\,U/[\omega\,(1-u_*^2)]$. The solution is controlled by the following nondimensional groups:

$$k_e = \frac{\pi c_e(1-u_*^2)}{6\,(1-\zeta_b)\,\delta\,Fr\sqrt{s-1}}\,,\; k_d = \frac{c_d(s-1)}{\delta\,Fr\,\tan\theta}\,,\; u_* = \sqrt{\frac{Sh_{cr}}{Sh}}\,,\; \mathcal{V} = \nu_t\,Fr\,(\tan\theta)^{3/2}\,,\; \mathcal{D} = \frac{D_u\,\tan\theta}{H\,V}\,.$$

The dispersion relation is obtained by setting the determinant of (28) to zero, i.e. $\mathbb{D}(k, \omega) \equiv |\overline{\overline{A}}| = 0$, to obtain a non-trivial solution. The dispersion relation links the complex wavenumber k with the complex frequency ω, and vice versa. Note that the nondimensional particle diffusion $\mathcal{D}$ increases the order of the characteristic polynomial (28) up to $O(k^2)$. For the set of values used in the numerical simulation of antidunes, we get $k_e = 0.0864$, $k_d = 4.52$, $u_* = 0.64$, $\mathcal{V} = 0.125$, $\mathcal{D} = 0.745$ and $\beta = 1$. The nondimensional wavenumber associated with the natural wavelength $\Lambda = 0.2$ m that grows spontaneously in the simulation is $k = 2\pi H/\Lambda \tan\theta = 9.36$ at the downstream reach of the flume and its corresponding temporal frequency in the linear stability analysis is $\omega_i = 0.044$ ($\omega_i V \tan\theta/H = 0.0674$ s^{-1}). This value is in close agreement with the numerical growth rate 0.068 s^{-1} obtained in Fig. 6(a). Furthermore, the dispersion relation serves to find the saddle points that explain the selection of a well-defined wavelength [70, 71].

We seek solutions to $\mathbb{D}(k_0, \omega_0) = 0$ and $\partial_k \mathbb{D}(k_0, \omega_0) = 0$ with $\partial_{kk} \mathbb{D}(k_0, \omega_0) \neq 0$ resulting from a pinch point between two spatial branches $k^+(\omega)$ and $k^-(\omega)$ originating from distinct halves of the k-plane with $k_{0,i} < 0$ (i.e. spatially growing solution) and $\omega_{0,i} > 0$ (i.e. temporal growing solution). In doing so, we ensure the zero group velocity condition $c_g = \partial\omega/\partial k = (\partial\mathbb{D}/\partial k)/(\partial\mathbb{D}/\partial\omega) = 0$, referred to as Briggs-Bers or Fainberg-Kurilko-Shapiro (in the Soviet literature) criterion [70, 71]. Hence the flow is absolutely unstable. Note that the increase in the order of the characteristic polynomial (28), $O(k^2)$, occurs with $\mathcal{D} > 0$ and favors the existence of mathematical solutions to the Briggs-Bers condition. In the presence of an absolute instability with just one saddle point, there are an absolute frequency and an absolute growth rate that determine the selective response of the system to perturbations. So, the system selects a natural frequency and consequently a unique saddle point wavenumber of the spatial branches among the wide range of unstable wavenumbers k. The response is dominated in this case by the mode with zero group velocity which grows in place, whilst the rest of the frequencies and wavenumbers are swept away by the flow [37]. In the presence of multiple saddle points, Pier and Peake [73] have shown that the theoretical calculation of the natural frequency and wavenumber is much more complicated. In our formulation, for the current set of nondimensional parameters, multiple saddles point exist at $k = -i\,1.197$ ($\omega = i\,0.0112$, Fig. 8(a)) and $k = 6.4 + i0.6$ ($\omega = 0.18 + i\,0.054$, Fig. 8(b)) with branches k^+ and k^- originating from distinct halves of the k-plane. The wavenumber selection occurs in the cross between a path connecting both saddle points and the real axis where $k_i = 0$ defining the maximum growth rate in the temporal stability analysis, which yields $k = 6.24$ and $\omega = 0.18 + i\,0.0536$. This point lies really close to the saddle point in Fig. 8(b) because it approaches the real axis. Consequently, the second saddle point controls bed instability over the first one that occurs in the imaginary axis [Fig. 8(a)]. The dimensional wavenumber in the numerical simulation $6.24 \leq 2\,\pi\,H/\Lambda\,\tan\theta \leq 9.3$ is in good agreement with the theoretical result $k = 6.24$. This demonstrates the accuracy of linear stability theory and the numerical simulations.

6. Concluding remmarks

In this article we investigated the problem of bedload transport in shallow water flows over erodible bottom slopes using the ensemble-averaged version of the stochastic-deterministic Saint-Venant-Exner equations (1)-(4b). According Einstein's theory [26], sediment transport results from the imbalance between the entrainment and deposition rates, $E = \lambda$ and $D = \kappa\,\langle\gamma\rangle$ in equation (7). The bulk sediment transport rate $\bar{q}_s = \bar{q}_{s,c} + \bar{q}_{s,d}$ defined by equation (6) is decomposed into the sum of the advection transport rate reflecting the driving action of water ($\bar{q}_{s,c} = \bar{u}_s\langle\gamma\rangle$) and the diffusive rate due to the spatial gradient of the mean particle activity ($\bar{q}_{s,d} = -D_u\partial_x\langle\gamma\rangle$) [9]. The diffusive nature of bedload transport and the influence of particle diffusion on transport rates have been reported experimentally for weak bedload transport as well as full mobility regime. In contrast with classical deterministic bedload transport theories, the sediment diffusion term $-D_u\partial_{xx}\langle\gamma\rangle$ in the mean particle activity equation (4b) results from the ensemble average of the stochastic Langevin equation (4a) for the Poisson density b.

There is a strong analogy between the ensemble-averaged sdSVE equations (3)-(4b) and the non-equilibrium sediment transport equations (17)-(18), also known as non-capacity or unsteady flux relaxation equations [27, 28, 37]. In the full mobility regime, the mean particle activity and the bulk sediment transport rate approach their steady state values $\langle\gamma\rangle = \langle\gamma\rangle_{ss}$ and $\bar{q}_s = \bar{q}_{ss}$, respectively, because at large Shields numbers, the leading-order terms in the advection diffusion equation (4b) are the source and sink terms λ and $-\kappa\langle\gamma\rangle$, see (23) for $Sh \gg Sh_{cr}$. The entrainment and deposition rates (13) were defined so that consistency with the equilibrium (or capacity) approach, which imposes $\bar{q}_s = \bar{q}_{ss}(Sh)$, is enforced. In weak/partial bedload transport, entrainment, deposition, convection and diffusion mechanisms compete with each other depending on the value of the adaptation length $l_{c,d}$ defined in equation (20) and the Péclet number $Pe = l_c/l_d = (\bar{u}_s^2/D_u\,\kappa)^{1/2}$. The prevalent mechanism of sediment transport is convection when $Pe \gg 1$—a limiting state in which the adaptation length $l_{c,d}$ tends to $l_c = \bar{u}_s/\kappa$—and diffusion when $Pe \ll 1$ and $l_{c,d} \approx l_d = \sqrt{D_u/\kappa}$. Next,an improved equation was proposed to evaluate the steady-state transport rate in the form $\bar{q}_s/\bar{q}_{s*} = (Sh/Sh_*)^{3/2}\,\Phi(Sh/Sh_*)$, which holds from the partial- to the full-mobility regimes. The master curve $\Phi(Sh/Sh_*)$ given by equation (25), see Fig. 2, closely matches the experimental data collected by Buffington [29] independently of sediment properties (that control the reference parameters Sh_* and $\bar{q}_{s*}$).

We ran numerical experiments for simulating shallow water flows over erodible sloping beds in laboratory flumes that produce nearly one-dimensional flows. The relative importance of the diffusive and advective transport rates was studied in the problem of degradation of a sloping channel (Test 3 in Newton [32]'s experiments) and for the unsteady flow that results from the development and migration of anti-dunes in gravel bed streams over steep slopes [33, 34, 35, 36]. On the whole, we found that both transport rates have the same order of magnitude at a certain stage of the bedload transport simulations.

In Newton's experiment the diffusive transport rate was dominant in the upstream reach of the flume in the early stage of the scouring process and vanished in the downstream reach of the channel where the flow was nearly uniform. In that reach, sediment particles were mainly advected by the flowing water when $x > 2-4\,l_{c,d}$, in agreement with the theoretical analysis of the adaptation length, which predicts the same lower bound for the flow to reach steady state. An excellent agreement was obtained between the numerical results and experimental data obtained by Newton [32], see Fig. 3, which provides further justification for the formulation and numerical implementation presented in this paper.

The nonlinear numerical simulation of anti-dunes on sloping bed reveals the capability of the ensemble-average sdSVE equations (3)-(4b) to predict upstream migrating bed forms with physically consistent wavelengths while the standard Exner equation (14) fails to produce such a result (bed is unconditionally stable for $Fr < 2$ [48]). Particle diffusion increases the order of the characteristic polynomial (28) to $O(k^2)$ when $\mathcal{D} > 0$, favours the existence of mathematical solutions to the Briggs-Bers condition and provokes absolute instability. Our numerical results are qualitatively consistent with the phenomenological description of the seminal experimental work done by Kennedy [74] who stated that: "the disturbance at the downstream end of the flume caused a train of waves to form" (p. 114) … "it was impossible to prevent large disturbances at the inlet" (p. 104). Indeed we observed wide fluctuations of the bed elevation and the bulk sediment transport rate near the inlet due to the migration of anti-dunes from the outlet to the inlet [Figs. 6-7].

At the end of the day, we firmly think that sediment diffusion cannot be left aside. Embodying diffusion into deterministic non-equilibrium sediment transport equations will likely improve the predictive capability of existing numerical codes. Furthermore, the computational cost of the depth-averaged sdSVE simulations is much lighter than previous rotational formulations based on the Navier-Stokes equations used for computing bed forms when using the standard Exner equation (14). We would like to highlight again that the versatile numerical framework described in this paper—and in [11]—makes it possible to use either deterministic or stochastic formulations of bed load transport within the same numerical framework.

Acknowledgments

Patricio Bohorquez acknowledges the financial support by CEACTierra (project #2013/00065/001), the Caja Rural Provincial de Jaén and the University of Jaén (project # UJA2014/07/04). Christophe Ancey was supported by the Swiss National Science Foundation under grant no. 200021-129538 and 200021-160083 (projects called "The Stochastic Torrent: stochastic model for bed load transport on steep slope").

Appendix A. Calibration of the model parameters in Newton's experiment

The calibration was done in four steps:

i. The initial water depth H, bed angle θ and water discharge Q were used to calibrate the bed roughness scaling factor k_s in the evaluation of the Darcy-Weisbach friction factor f, which in fully developed turbulent flow and rough regime takes the form [75]

$$\frac{1}{\sqrt{f}} = -2\,\log_{10}\left(\frac{k_s\,\delta^2}{3.71}\right)\,. \tag{A.1}$$

Upon substituting (A.1) into equation (8) and solving for the scaling factor, we get $k_s \approx 4$, which was kept constant during the numerical simulation. Following Bohorquez and Ancey [11], we computed the sediment velocity as

$$\bar{u}_s = \beta\,\bar{v} \quad \text{with} \quad \beta \equiv \min\left(1.44\sqrt{\frac{f}{8\,Sh_{cr}}}, 1\right)\,. \tag{A.2}$$

Note that during the numerical simulation the parameter δ^2 increases due to the higher flow depths developing at shallower slopes as time proceeds, modifying both f (A.1) and β (A.2).

ii. Then we calibrated the critical Shields number Sh_{cr} for the onset of sediment motion by fitting the solid discharge at the outlet of the flume (circles in Fig. 3(c)) as a function of the mean bed slope (corresponding to the experimental thalweg in Fig. 3(a)), which gives $\bar{q}_{ss} = 6.85\,\theta - 0.005$. This step requires some algebraical manipulations and iterative solution of the equations that are not reported for the sake of brevity. The critical angle of equilibrium is thus $\theta_{cr} = 0.042°$. Taking into account that the water discharge was kept constant in Newton's experiment, using (8), (9) and (A.1), we get the critical Shields number $Sh_{cr} = 0.0441$ for the theoretical grain-size to water-depth ratio $\delta^2 = 0.009$.

iii. The next parameter that requires calibration is the deposition rate $\kappa = c_d\sqrt{(s-1)\,g/d}$ or, equivalently, the nondimensional parameter c_d [11]. To be consistent with previous non-equilibrium numerical simulations of Newton's degradation experiment [52, 38], we have estimated the deposition rate from the convective

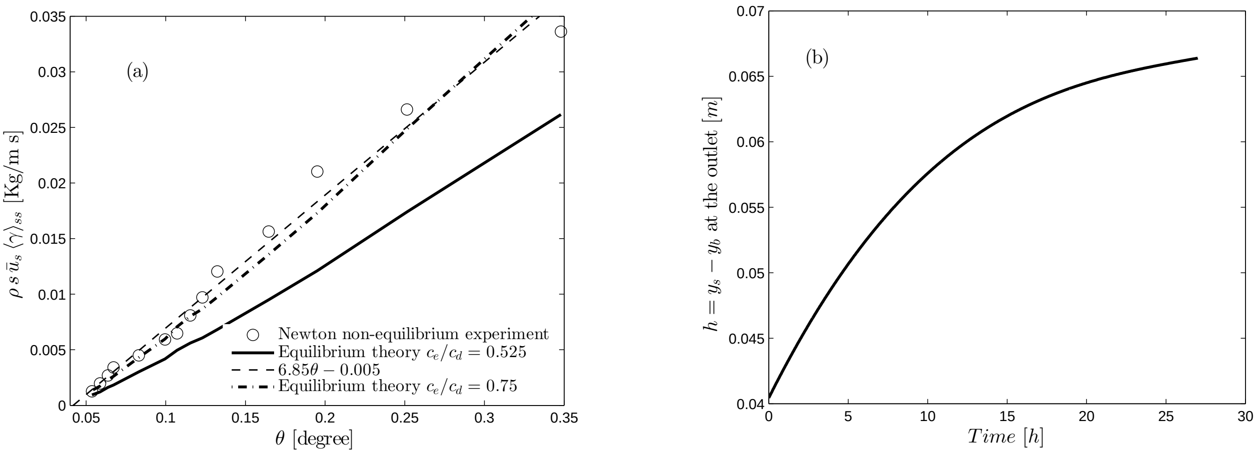

Figure A.9: Calibration of the critical Shields number Sh_{cr} (or critical slope angle θ_{cr}) and the depth at the flume outlet in Newton's experiment. Both figures were constructed using available experimental data (see solid circles in Fig. 3) in the downstream reach of the flume ($x > 6\ m$) for the constant water discharge $Q = 0.0057$ m^3/s under uniform flow condition. The parameter $Sh_{cr} = 0.0441$ is used in the numerical simulation to evaluate $\{\beta, \bar{u}_s\}$—see equation (A.2)—and $\{\lambda, \langle\gamma\rangle_{ss}\}$—see equation (A.3). The nondimensional erosion-to-deposition ratio $c_e/c_d = 0.525$ was used in the non-equilibrium numerical simulation. Good agreement with the experimental results is obtained when the sediment diffusion is included in the modelling, as shown in Fig. 3. Plot (b) was constructed by solving equations (8) and (A.1) for h and by varying the slope $\tan\theta$ with time according to the experiments.

adaptation length ℓ_c as $\kappa = \bar{u}_s/\ell_c$. Taking into account the scaling proposed by Charru [37] for turbulent flows, we obtain $c_d = \bar{u}_s\sqrt{d}/\sqrt{(s-1)\, g\, \ell_c^2}$. Wu and Wang [52], El Kadi Abderrezzak and Paquier [38] and Zhang et al. [39] adopted $\ell_c \approx 1$ m. Surprisingly, by setting $\ell_c \sim 1$ m, we get $c_d \sim O(10^{-3})$ in Newton's setup that is much lower than the constant value of $c_d = 0.1$ proposed by Lajeunesse et al. [40]. We fixed $c_d = 1.6 \times 10^{-3}$ in our computations.

iv. Following Charru [37] and Bohorquez and Ancey [11], we fix the erosion rate λ so that achieve the steady-state particle activity can be reached during the simulation.

$$\langle\gamma\rangle_{ss} = \frac{\lambda}{\kappa} = \frac{c_e\, V_p}{c_d\, d^2}\, (Sh - Sh_{cr})\ , \tag{A.3}$$

where $V_p = \pi d^3/6$ is the typical particle volume. Figure A.9(a) shows a comparison of the solid discharge in Newton's experiments and our theoretical prediction in uniform regime with $c_e = 8.4 \times 10^{-4}$. For this value of c_e, steady state theory for uniform flow underestimates the experimental bed load transport rate in the non-equilibrium degradation experiment. This is not a shortcoming of non-equilibrium bed load theory because the total sediment load transport rate increases due to the contributions of sediment diffusion and flow unsteadiness, as described in Section 5.1.

References

[1] J. D. Wilson, B. L. Sawford, Review of Lagrangian stochastic models for trajectories in the turbulent atmosphere, Boundary-Lay. Meteorol. 78 (1996) 191–210.

[2] J. J. H. Brouwers, Statistical description of turbulent dispersion, Phys. Rev. E 86 (2012) 066309.

[3] V. Nikora, H. Habersack, T. Huber, I. McEwan, On bed particle diffusion in gravel bed flows under weak bed load transport, Water Resour. Res. 38 (2002) WR000513.

[4] V. Ganti, M. Meerschaert, E. Foufoula-Georgiou, E. Viparelli, G. Parker, Normal and anomalous dispersion of gravel tracer particles in rivers, J. Geophys. Res. 115 (2010) F00A12.

[5] R. Martin, D. Jerolmack, R. Schumer, The physical basis for anomalous diffusion in bed load transport, J. Geophys. Res. 117 (2012) F01018.

[6] J. Roseberry, M. Schmeeckle, D. Furbish, A probabilistic description of the bed load sediment flux: 2. Particle activity and motions, J. Geophys. Res. 117 (2012) F03032.

[7] J. Heyman, H. B. Ma, F. Mettra, C. Ancey, Spatial correlations in bed load transport: Evidence, importance, and modeling, J. Geophys. Res. 119 (2014) 1751–1767.

[8] G. Seizilles, E. Lajeunesse, O. Devauchelle, M. Bak, Cross-stream diffusion in bedload transport, Phys. Fluids 26 (2014) 013302.

[9] D. J. Furbish, P. K. Haff, J. C. Roseberry, M. W. Schmeeckle, A probabilistic description of the bed load sediment flux: 1. Theory, J. Geophys. Res. 117 (2012) F03031.

[10] C. Ancey, J. Heyman, A microstructural approach to bed load transport: mean behaviour and fluctuations of particle transport rates, J. Fluid Mech. 744 (2014) 129–168.

[11] P. Bohorquez, C. Ancey, Stochastic-deterministic modeling of bed load transport in shallow water flow over erodible slope: Linear stability analysis and numerical simulation, Adv. Water Resour. 83 (2015) 36–54.

[12] G. K. Gilbert, The transportation of débris by running water, U.S. Geol. Surv. Prof. Pap. 86 (1914) 263 pp.

[13] D. B. Simons, E. V. Richardson, Forms of bed roughness in alluvial channel, J. Hydraul. Div. Am. Soc. Civ. Eng. 87 (1961) 87–105.

[14] J. Kennedy, The formation of sediment ripples, dunes, and antidunes, Annu. Rev. Fluid Mech. 1 (1969) 147–168.

[15] J. P. Soni, R. J. Garde, K. G. Ranga Raju, Aggradation in streams due to overloading, J. Hydraul. Div. Am. Soc. Civ. Eng. 106 (1980) 117–132.

[16] C. Ancey, T. Böhm, M. Jodeau, P. Frey, Statistical description of sediment transport experiments, Phys. Rev. E 74 (2006) 011302.

[17] S. Naqshband, J. S. Ribberink, D. Hurther, S. J. M. H. Hulscher, Bed load and suspended load contributions to migrating sand dunes in equilibrium, J. Geophys. Res. Earth Surf. 119 (2014) 1043–1063.

[18] M. J. B. Cartigny, D. Ventra, G. Postma, J. H. van Den Berg, Morphodynamics and sedimentary structures of bedforms under supercritical-flow conditions: New insights from flume experiments, Sedimentology 61 (2014) 712–748.

[19] E. M. Yager, M. Kenworthy, A. Monsalve, Taking the river inside: Fundamental advances from laboratory experiments in measuring and understanding bedload transport processes, Geomorphology doi:10.1016/j.geomorph.2015.04.002 (2015).

[20] M. H. García, Sediment transport and morphodynamics, in: M. H. García (Ed.), Sedimentation Engineering, volume ASCE Manuals and Reports on Engineering Practice 110, American Society of Civil Engineers, Reston, 2007, pp. 21–164.

[21] M. Colombini, A decade's investigation of the stability of erodible stream beds, J. Fluid Mech. 756 (2014) 1–4.

[22] C. Gardiner, M. Steyn-Ross, Adiabatic elimination in stochastic systems. II. Application to reaction diffusion and hydrodynamic-like systems, Phys. Rev. A 29 (1984) 2823.

[23] C. Ancey, Stochastic modeling in sediment dynamics: Exner equation for planar bed incipient bed load transport conditions, J. Geophys. Res. 115 (2010) F00A11.

[24] D. Furbish, A. Ball, M. Schmeeckle, A probabilistic description of the bed load sediment flux: 4. Fickian diffusion at low transport rates, J. Geophys. Res. 117 (2012) F03034.

[25] F. Ballio, V. Nikora, S. Coleman, On the definition of solid discharge in hydro-environment research and applications, J. Hydraul. Res. 52 (2014) 173–184.

[26] H. Einstein, The bed-load function for sediment transportation in open channel flows, Technical Report Technical Report No. 1026, United States Department of Agriculture, 1950.

[27] W. Wu, Computational River Dynamics, Taylor & Francis, London, 2007.

[28] Z. Cao, Z. Li, G. Pender, P. Hu, Non-capacity or capacity model for fluvial sediment transport, Water Manage. 165 (2010) 193–211.

[29] J. Buffington, The legend of A. Shields, J. Hydraul. Eng. 125 (1999) 376–387.

[30] N. Cheng, Exponential formula for bedload transport, J. Hydraul. Eng. 128 (2002) 942–946.

[31] P. R. Wilcock, J. C. Crowe, Surface-based transport model for mixed-size sediment, J. Hydraul. Eng. 129 (2003) 120–128.

[32] C. T. Newton, An experimental investigation of bed degradation in an open channel, Trans. Boston Society of Civil Engineers (1951) 28–60.

[33] H. H. Cao, Resistance hydraulique d'un lit à gravier mobile à pente raide; étude expérimentale, Ph.D. thesis, EPFL, Switzerland, 1985. http://dx.doi.org/10.5075/epfl-thesis-589.

[34] J. C. Bathurst, W. H. Graf, H. H. Cao, Bedload discharge equations for steep mountain rivers, in: C. R. Thorne, J. C. Bathurst, R. D. Hey (Eds.), Sediment Transport Equations in Gravel-Bed Rivers, Wiley, Chichester, 1987, pp. 453–491.

[35] A. Recking, V. Bacchi, M. Naaim, P. Frey, Antidunes on steep slopes, J. Geophys. Res. 114 (2009) F04025.

[36] F. Mettra, Morphodynamic mechanisms in steep channels: from local processes to large-scale evolution, Ph.D. thesis, LHE/EPFL, 2014. http://dx.doi.org/10.5075/epfl-thesis-6065.

[37] F. Charru, Hydrodynamic Instabilities, Cambridge University Press, Cambridge, 2011.

[38] K. El Kadi Abderrezzak, A. Paquier, One-dimensional numerical modeling of sediment transport and bed deformation in open channels, Water Resour. Res. 45 (2009) W05404.

[39] S. Zhang, J. G. Duan, M. Strelkoff, Grain-scale nonequilibrium sediment-transport model for unsteady flow, J. Hydraul. Eng. 139 (2012) 22–36.

[40] E. Lajeunesse, L. Malverti, F. Charru, Bed load transport in turbulent flow at the grain scale: Experiments and modeling, J. Geophys. Res. 115 (2010) F04001.

[41] Z. Cao, R. Day, S. Egashira, Coupled and decoupled numerical modeling of flow and morphological evolution in alluvial rivers, J. Hydraul. Eng. 128 (2002) 306–321.

[42] H. Einstein, Der Geschiebetrieb als Wahrscheinlichkeitproblem (Bedload transport as a probability problem), (english translation by W. W. Sayre, in Sedimentation (Symposium to honor H. A. Einstein), edited by H. W. Shen, Fort Collins, Colorado, 1972, C1–C105, ETHZ, 1937.

[43] P.-Y. Julien, Erosion and Sedimentation, 2nd ed., Cambridge University Press, Cambridge, 2010.

[44] N.-S. Cheng, Y.-M. Chiew, Analysis of initiation of sediment suspension from bed load, J. Hydraul. Eng. 125 (1999) 855–861.

[45] M. Elhakeem, J. Imran, Density functions for entrainment and deposition rates of uniform sediment, J. Hydraul. Eng. 133 (2007) 917–926.

[46] F. Exner, Ueber die Wechselwirkung zwischen Wasser und Geschiebe in Fluessen, Sitzungsberichte der kaiserlichen Akademie der Wissenschaften Wien, Abteilung IIa 134 (1925) 165–205.

[47] F. Charru, Selection of the ripple length on a granular bed sheared by a liquid flow, Phys. Fluids 18 (2006) 121508.

[48] N. J. Balmforth, A. Provenzale, Patterns of dirt, in: N. J. Balmforth, A. Provenzale (Eds.), Geomorphological Fluid Mechanics, Springer Verlag, Berlin, 2001, pp. 369–393.

[49] J. Li, M. Qi, Local scour induced by upstream riverbed level lowering, Nat. Hazards 77 (2015) 1811–1827.

[50] B. C. Phillips, A. J. Sutherland, Spatial lag effects in bed load sediment transport, J. Hydraul. Res. 427 (1989) 115–133.

[51] Z. Cao, G. Pender, S. Wallis, P. A. Carling, Computational dam-break hydraulics over erodible bed, J. Hydraul. Eng. 130 (2004) 689–703.

[52] W. Wu, S. Wang, One-dimensional explicit finite-volume model for sediment transport, J. Hydraul. Res. 46 (2008) 87–98.

[53] C. Ancey, A. C. Davison, T. Böhm, M. Jodeau, P. Frey, Entrainment and motion of coarse particles in a shallow water stream down a steep slope, J. Fluid Mech. 595 (2008) 83–114.

[54] G. Parker, Y. Fukushima, H. Pantin, Self-accelerating turbidity currents, J. Fluid Mech. 171 (1986) 145–181.

[55] P. Bohorquez, R. Fernandez-Feria, Transport of suspended sediment under the dam-break flow on an inclined plane bed of arbitrary slope, Hydrolog. Process. 22 (2008) 2615–2633.

[56] B. Greimann, Y. Lai, J. Huang, Two-dimensional total sediment load model equations, J. Hydraul. Eng. 134 (2008) 1142–1146.

[57] H. Sun, D. Chen, Y. Zhang, L. Chen, Understanding partial bed-load transport: Experiments and stochastic model analysis, J. Hydrol. 521 (2015) 196–204.

[58] T. Drake, R. Shreve, W. Dietrich, L. Leopold, Bedload transport of fine gravel observed by motion-picture photography, J. Fluid Mech. 192 (1988) 193–217.

[59] K. Ramos, S. Gibson, L. Kavvas, R. Heath, J. Sharp, Estimating bed-load advection and dispersion coefficients with the method of moments, World Environmental and Water Resources Congress 2015 (2015) 1736–1741.

[60] S. Jain, Note on lag in bedload discharge, J. Hydraul. Eng. 118 (1992) 904–917.

[61] A. J. Bagnold, The movement of desert sand, Proc. R. Soc. London ser. A 157 (1936) 594–620.

[62] R. Fernandez Luque, R. van Beek, Erosion and transport of bed-load sediment, J. Hydraul. Res. 14 (1976) 127–144.

[63] M. S. Yalin, A. M. F. da Silva, Fluvial Processes, IAHR Monograph, IAHR, Delft, The Netherlands, 2001.

[64] R. Bagnold, The flow of cohesionless grains in fluids, Proc. R. Soc. London 249 (1956) 235–296.

[65] S. Gottlieb, D. I. Ketcheson, C.-W. Shu, High order strong stability preserving time discretizations, J. Sci. Comput. 38 (2009) 251–289.

[66] D. I. Ketcheson, M. Parsani, R. J. LeVeque, Higher order wave propagation algorithms for hyperbolic systems, SIAM J. Sci. Comput. 35 (2013) A351–A377.

[67] E. Blayo, L. Debreu, Revisiting open boundary conditions from the point of view of characteristic variables, Ocean Modelling 9 (2005) 231–252.

[68] F. Comiti, L. Mao, Recent advances in the dynamics of steep channels, in: M. Church, P. M. Baron, A. G. Roy (Eds.), Gravel-bed rivers: Processes, tools, environments, 2012, pp. 351–377.

[69] M. Colombini, Revisiting the linear theory of sand dune formation, J. Fluid Mech. 502 (2004) 1–16.

[70] P. J. Schmid, D. S. Henningson, Stability and Transition in Shear Flows, Springer, 2001.

[71] M. P. Juniper, A. Hanifi, V. Theofilis, Modal stability theory, Appl. Mech. Rev. 66 (2014) 024804.

[72] J. W. Lavelle, W. C. Thacker, A pretty good sponge: Dealing with open boundaries in limited-area ocean models, Ocean Modelling 20 (2008) 270–292.

[73] B. Pier, N. Peake, Global modes with multiple saddle points, European Journal of Mechanics, B/Fluids 49 (2015) 335–344.

[74] J. F. Kennedy, Stationary waves and antidunes in alluvial channel, Ph.D. thesis, California Institute of Technology. Pasadena, California, 1960.

[75] C. F. Colebrook, Turbulent flow in pipes with particular reference to the transition region between the smooth- and rough-pipe laws, J. Inst. Civ. Eng. 11 (1939) 133–156.